Earth, Planets and Space

FULL PAPER Open Access

Development of a kinematic GNSS-Acoustic positioning method based on a state-space model

Fumiaki Tomita[1,2*], Motoyuki Kido[3], Chie Honsho[4] and Ryo Matsui[4]

Abstract

GNSS-A (combination of Global Navigation Satellite System and Acoustic ranging) observations have provided important geophysical results, typically based on static GNSS-Acoustic positioning methods. Recently, continuous GNSS-Acoustic observations using a moored buoy have been attempted. Precise kinematic GNSS-Acoustic positioning is essential for these approaches. In this study, we developed a new kinematic GNSS-A positioning method using the extended Kalman filter (EKF). As for the observation model, parameters expressing underwater sound speed structure [nadir total delay (NTD) and underwater delay gradients] are defined in a similar manner to the satellite geodetic positioning. We then investigated the performance of the new method using both the synthetic and observational data. We also investigated the utility of a GNSS-Acoustic array geometry composed of multi-angled transponders for detection of vertical displacements. The synthetic tests successfully demonstrated that (1) the EKF-based GNSS-Acoustic positioning method can resolve the GNSS-Acoustic array displacements, as well as NTDs and underwater delay gradients, more precisely than those estimated by the conventional kinematic positioning methods and (2) precise detection of vertical displacements can be achieved using multi-angled transponders and EKF-based GNSS-Acoustic positioning. Analyses of the observational data also demonstrated superior performance of the EKF-based GNSS-Acoustic positioning method, when assuming a laterally stratified sound speed structure. Further, we found three superior aspects to the EKF-based array positioning method when using observational data: (1) robustness of the solutions when some transponders fail to respond, (2) precise detection for an abrupt vertical displacement, and (3) applicability to real-time positioning when sampling interval of the acoustic ranging is shorter than 30 min. The precision of the detection of abrupt steps, such as those caused by coseismic slips, is ~ 5 cm (1σ) using this method, an improvement on the precision of ~ 10 cm of conventional methods. Using the observational data, the underwater delay gradients and the horizontal array displacements could not be accurately solved even using the new method. This suggests that short-wavelength spatial heterogeneity exists in the actual ocean sound speed structure, which cannot be approximated using a simple horizontally graded sound speed structure.

Keywords: GNSS-A positioning, Seafloor geodesy, Extended Kalman filter, Real-time positioning

Introduction

The GNSS-Acoustic (GNSS-A) positioning method, which was contrived by the Scripps Institute of Oceanography (Spiess 1985; Spiess et al. 1998), is a combination technique of kinematic GNSS positioning on a sea surface platform and underwater acoustic ranging between the sea-surface platform and a seafloor acoustic benchmark (Fig. 1). The GNSS-A observations enable measurement of seafloor displacements in a global geodetic coordinate system. The system has provided important geodetic observation results including detection of interseismic (e.g., Gagnon et al. 2005; Tadokoro et al. 2012; Yokota et al. 2016), coseismic (e.g., Tadokoro et al.

*Correspondence: tomitaf@jamstec.go.jp
[2] Present Address: Japan Agency for Marine-Earth Science and Technology, Yokohama, Japan
Full list of author information is available at the end of the article

2006; Sato et al. 2011; Kido et al. 2011), and postseismic (e.g., Watanabe et al. 2014; Tomita et al. 2015, 2017; Honsho et al. 2019) deformation associated with earthquake cycles in subduction zones, and plate motions near ridge-transform boundaries (Chadwell and Spiess 2008).

Although GNSS-A observations are typically collected by campaign-style surveys using a research vessel as the sea surface platform, continuous GNSS-A observations have recently been developed using moored buoys (e.g., Imano et al. 2015; Kido et al. 2018; Kato et al. 2018; Imano et al. 2019) for an early warning system through instant offshore geodetic positioning. To support these efforts, we investigate a precise "kinematic" GNSS-A positioning method. Most recently developed GNSS-A positioning methods were designed as a "static" positioning method, estimating a single positioning solution using long-term (over several hours) campaign survey data (e.g., Fujita et al. 2006; Ikuta et al. 2008; Honsho and Kido 2017; Yokota et al. 2018). Although the classic GNSS-A positioning method (Spiess et al. 1998; Kido et al. 2006) can be used to estimate a kinematic solution from a single acoustic ping, each solution has tens of centimeters of positioning error due to spatio-temporal fluctuations in the underwater sound speed structure (SSS). However, it should be noted that it is possible to obtain a comparable solution with static GNSS-A positioning by averaging the kinematic solutions from long-term observational data (e.g., Kido et al. 2006; Tomita et al. 2015). Furthermore, the kinematic positioning method is useful for the detection of temporally noisy data and for determining a final solution without using the noisy data. Thus, the classic positioning method is still an effective technique and has provided important observational results (e.g., Gagnon et al. 2005; Tomita et al. 2017).

As noted above, a major source of GNSS-A positioning error is thought to be the spatio-temporal fluctuations in underwater SSS. In past studies, a laterally stratified SSS has been assumed, and this assumption is generally applicable (e.g., Kido et al. 2008). If horizontal heterogeneity in SSS is present, systematic positioning errors will arise. Additional file 1: Figure S1 shows a schematic image that a horizontally graded SSS (simple case of the horizontal heterogeneity in SSS) produces systematic bias in positioning results. As a response to this, static

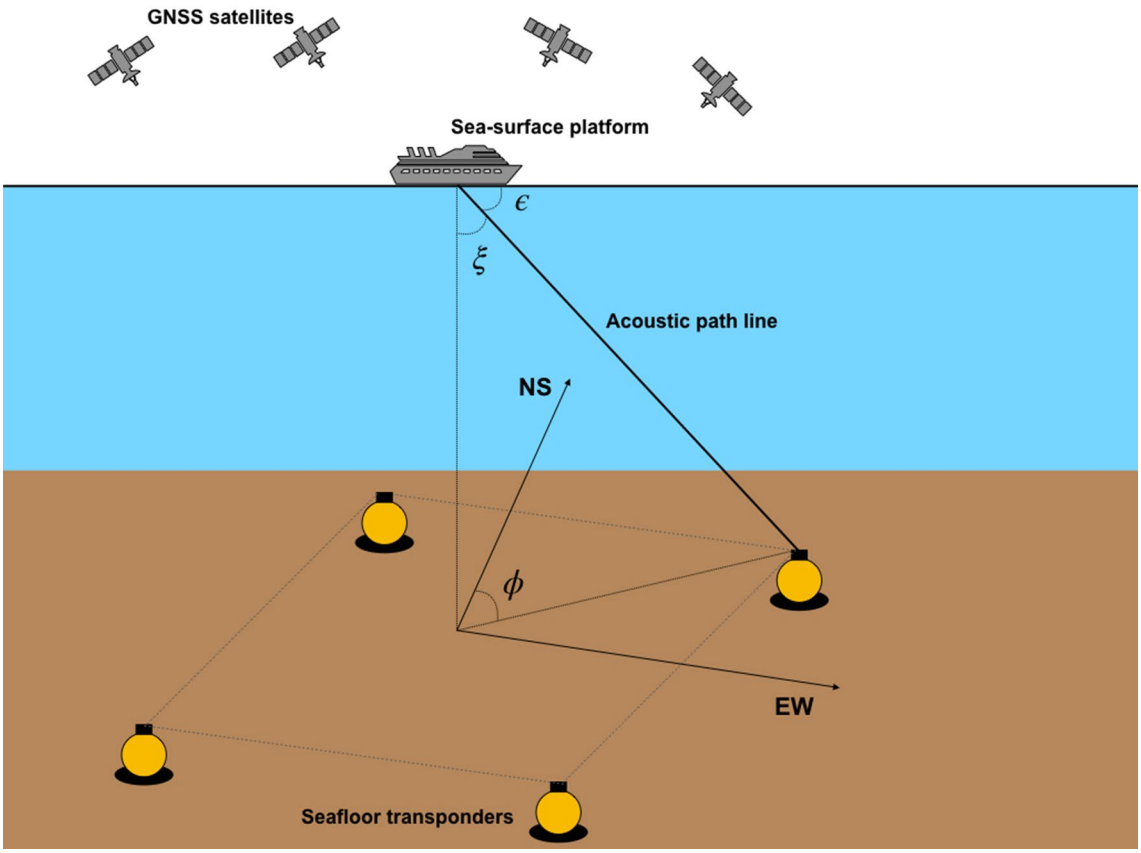

Fig. 1 Schematic image of the GNSS-Acoustic observation system. Schematic image of a GNSS-A observation system is shown; inclination angle (ϵ), shot angle (ξ), and azimuth for the seafloor transponder (ϕ) are used in equations in the main text

GNSS-A positioning methods that consider the horizontally graded structure of underwater sound speeds that are persistent over the long-term (over several hours) have recently been developed (e.g., Yasuda et al. 2017; Yokota et al. 2018; Honsho et al. 2019), and have demonstrated some reduction in biased positioning errors. However, it has been found that short-term fluctuations in the horizontal heterogeneity of the SSS can be caused by internal gravitational waves (e.g., Spiess et al. 1998; Kido et al. 2006; Tomita et al. 2015), and these short-term fluctuations have degraded the precision of the kinematic GNSS-A positioning method.

In this study, we attempt to develop a kinematic GNSS-A positioning method based on a state-space model using the extended Kalman filter (EKF) (Kalman 1960) to improve the precision of the kinematic GNSS-A positioning method. The Kalman filter (KF) has frequently been used in GNSS positioning systems to precisely estimate GNSS antenna position, tropospheric delay, ionospheric delay and other parameters (e.g., Lichten and Border 1987). Since the KF can constrain the behavior of time-dependent unknown parameters based on a given stochastic processes, it is a useful tool for kinematic inversion techniques. In this study, we first formulate the spatio-temporal fluctuations in the SSS for the GNSS-A positioning, based on the formulation for the tropospheric delay in the satellite geodetic measurements. Subsequently, we apply the above formulation to the EKF framework. Then we investigate the performance of this EKF-based approach using synthetic tests, and finally we apply the approach to observational data from the off-Tohoku region (northeast Japan).

Method

Principles of the GNSS-A positioning method

A conceptual model of the GNSS-A observation system is shown in Fig. 1. The seafloor benchmark for each GNSS-A observation site is composed of several (~ 3–6) transponders forming a triangular- or square-shaped array. In the surveys, first, the position of a GNSS antenna attached to the sea-surface platform was measured using a kinematic GNSS positioning technique. We then determined the position of an acoustic transducer attached to the sea-surface platform from the GNSS antenna positions, the relative position between the GNSS antenna and the acoustic transducer, and the attitude of the sea-surface platform. As well as positioning the acoustic transducer, the acoustic transducer transmits an acoustic signal and receives the returned acoustic signal from the seafloor transponders; thus, round-trip travel times between the sea-surface acoustic transducer and the seafloor transponders were obtained. We finally estimated the positions of the seafloor transponders by an iterative non-linear least means square technique minimizing residuals between the observed travel times and the calculated travel times (e.g., Spiess et al. 1998; Kido et al. 2006; Fujita et al. 2006; Ikuta et al. 2008).

One of the most important assumptions of the GNSS-A analysis is the rigid movement of the seafloor transponder array. Since an individual seafloor transponder position can be estimated using the acoustic travel-time data collected by a "moving survey" (the acoustic pings are transmitted from various sea-surface points) (e.g., Ikuta et al. 2008; Honsho and Kido 2017; Additional file 1: Figure S2a), as similar to the determination of the seismological hypocenter (e.g., Hirata and Matsu'ura 1987), we can determine array geometry composed of the transponders. Then, constraining the array geometry, array displacements relative to the predetermined array position can be precisely estimated (e.g., Spiess et al. 1998; Kido et al. 2006; Matsumoto et al. 2008; Honsho and Kido 2017; Chen et al. 2018; Tadokoro et al. 2018b). If the array geometry is well determined, an array displacement can be estimated using only a single acoustic ping which simultaneously transmits to all seafloor transponders (e.g., Spiess et al. 1998; Kido et al. 2006; Additional file 1: Figure S2b). This type of the GNSS-A positioning, using individual pings, previously introduced as the classic GNSS-A positioning method in "Introduction" and often called "array positioning", can in principle be achieved using the kinematic GNSS-A positioning method. Note that observational data collected from "point surveys" (where the acoustic pings are transmitted from the center of the seafloor transponder array) are required for kinematic GNSS-A positioning because accuracy of the array displacements degrades away from the array center (e.g., Kido 2007; Imano et al. 2015, 2019). In the following sections, we introduce a kinematic GNSS-A positioning method based on array positioning where the array geometry is already determined.

The observation equation analogy to satellite measurements

In this section, observation equations for the kinematic array positioning method are introduced. This method assumes either a laterally stratified SSS or a horizontally graded SSS. For the method assuming a laterally stratified SSS, we utilize a concept of nadir total delay (NTD) for expressing the temporal fluctuation in the average sound speed, following Kido et al. (2008) and Honsho and Kido (2017). The NTD corresponds to the zenith total delay (ZTD) that expresses tropospheric delay in the satellite geodetic measurements (e.g., Marini 1972). For the

method assuming a horizontally graded SSS, we formulated the underwater delay gradient of sound speed based on the azimuthal dependence, as similar to the expression of the tropospheric delay gradient in the satellite geodetic measurements (e.g., MacMillan 1995).

For the assumption of a laterally stratified SSS, the observation equation expressing a round-trip travel time for the seafloor transponder k at time t_n is written as follows:

$$T_{k,n}^{\mathrm{obs}} = T_{k,n}^{\mathrm{cal}}(\mathbf{p}_k + \delta\mathbf{p}_n; \mathbf{d}_n; \nu_0) + M(\epsilon_{k,n})NTD_n \quad (1)$$

with

$$\mathbf{p}_k = \left(p_k^{\mathrm{EW}}, p_k^{\mathrm{NS}}, p_k^{\mathrm{Z}}\right)^{\mathrm{T}}, \quad (2)$$

$$\delta\mathbf{p}_n = \left(\delta p_n^{\mathrm{EW}}, \delta p_n^{\mathrm{NS}}, \delta p_n^{\mathrm{Z}}\right)^{\mathrm{T}}, \quad (3)$$

where $T_{k,n}^{\mathrm{obs}}$ and $T_{k,n}^{\mathrm{cal}}$ represent an observed and calculated travel time, respectively. The travel time is calculated from the initial transponder position, $\mathbf{p}_k$, and the array displacement, $\delta\mathbf{p}_n$. $\mathbf{d}_n$ represents the position of a sea-surface acoustic transducer at time t_n and ν_0 represents the initial sound speed profile. NTD_n represents the NTD for time t_n and $M(\epsilon_{k,n})$ represents the mapping function for NTD, which depends on an inclination angle $\epsilon_{k,n}$ of the acoustic ray path (Fig. 1). In this study, we adopted a simple mapping function using the sin function (Marini 1972):

$$M(\epsilon_{k,n}) = \frac{1}{\sin\epsilon_{k,n}}\left(= \frac{1}{\cos\xi_{k,n}}\right). \quad (4)$$

This mapping function can also be represented using a shot angle of the acoustic ray path, $\xi_{k,n}$, which is the same formulation of the array positioning introduced by Kido et al. (2006, 2008). In Eq. (1), the unknown parameters for each time step are the three-dimensional array displacement, $\delta\mathbf{p}_n$, and NTD. This observation equation is similar to that presented in Kido et al. (2006, 2008), but we newly introduced a vertical component for the array displacement, δp_n^{Z}, as an unknown parameter. The vertical array displacement cannot be determined from kinematic array positioning using the point survey data at conventional GNSS-A sites because of the trade-off between vertical array displacements and the changes in sound speed (NTDs) (Additional file 1: Figure S3a). Thus, the conventional kinematic array positioning method fixes the vertical motion and estimates only the horizontal motions. Meanwhile, it is known that the moving survey data are essential to detect displacements in the vertical component (e.g., Sato et al. 2013) because the variation in shot angle of the seafloor transponders obtained from the moving survey is required to solve the trade-off relationship. At some recent GNSS-A observation sites, six transponders have been used to form a combination of small and large triangular arrays (Kido et al. 2015), providing variation in the shot angles even for a point survey (Additional file 1: Figure S3b). Thus, we can detect the vertical array displacement even when using kinematic array positioning for a site with "multi-angled transponders". The effects of using the multi-angled transponders are investigated in "Synthetic test" and "Application".

For the assumption of a horizontally graded sound speed structure, the observation equation expressing a round-trip travel time for the seafloor transponder, k, at time, t_n, is written as follows:

$$T_{k,n}^{\mathrm{obs}} = T_{k,n}^{\mathrm{cal}}(\mathbf{p}_k + \delta\mathbf{p}_n; \mathbf{d}_n; \nu_0) + M(\epsilon_{k,n})NTD_n + M(\epsilon_{k,n})\cot\epsilon_{k,n}\left(G_n^{\mathrm{EW}}\sin\phi_{k,n} + G_n^{\mathrm{NS}}\cos\phi_{k,n}\right), \quad (5)$$

where G_n^{EW} and G_n^{NS} represent the underwater delay gradients for the east–west and north–south components, respectively. $\phi_{k,n}$ is the azimuth of the seafloor transponder from the sea-surface platform at time, t_n. This formulation for the underwater delay gradient is the same as that for the tropospheric delay gradient in the satellite geodetic measurements (MacMillan 1995). Although Kido (2007) proposed a formulation for describing the contributions to the sound speed gradient similar to our own formulation, the formulation of Kido (2007) did not account for the effect related to each seafloor transponder depth, represented by $\cot\epsilon_{k,n}$ in Eq. (5). Thus, our formulation is an updated version of Kido (2007). Yasuda et al. (2017) and Yokota et al. (2018) present alternative formulations for the sound speed gradient. However, their formulations necessitate that the acoustic ranging data must be collected from various sea-surface shot points by moving the sea-surface platform; therefore, they are unsuitable for use in kinematic positioning. Our formulation is suitable for use in kinematic positioning, but it should be noted that the sea-surface platform should be kept in position above the array center to obtain good resolution as pointed out by Kido (2007).

Application to the extended Kalman filter

We apply the above observation equation for the kinematic GNSS-A positioning to EKF. Since an inversion problem in the GNSS-A positioning is non-linear, EKF is utilized in this study. This non-linear state space model is governed by a system model (state transition equation) defined as

$$\mathbf{x}_{n+1} = \mathbf{F}_n(\mathbf{x}_n) + \mathbf{u}_n + \mathbf{v}_n \quad (6)$$

and the observation model (observation equation) is defined as

$$\mathbf{y}_n = \mathbf{H}_n(\mathbf{x}_n) + \mathbf{w}_n, \tag{7}$$

where $\mathbf{y}_n$ and $\mathbf{x}_n$ are the observation vector and the state vector at time, t_n, respectively. $\mathbf{u}_n$ is the control input vector, $\mathbf{v}_n$ is the process noise vector and $\mathbf{w}_n$ is the measurement error vector. Since the EKF assumes that the processing noise and measurement errors follow the Gaussian distribution, their probability density functions are denoted as follows:

$$p(\mathbf{v}_n) \sim N(\mathbf{0}, \mathbf{Q}_n) \tag{8}$$

and

$$p(\mathbf{w}_n) \sim N(\mathbf{0}, \mathbf{R}_n). \tag{9}$$

The process noise vector, $\mathbf{v}_n$, is under the Gaussian noise with average zero and the covariance matrix (the process noise matrix), $\mathbf{Q}_n$. The measurement error, $\mathbf{w}_n$, is under the Gaussian noise with average zero and the covariance matrix, $\mathbf{R}_n$. $\mathbf{F}_n$ and $\mathbf{H}_n$ in Eqs. (6) and (7) are the non-linear functions for calculating the state transition and the synthetic observations from the state parameters, respectively. When a linear state space model is assumed for the system model, Eq. (6) is reformulated using a linear transition matrix, $\bar{\mathbf{F}}_n$, as follows:

$$\mathbf{x}_{n+1} = \bar{\mathbf{F}}_n \mathbf{x}_n + \mathbf{u}_n + \mathbf{v}_n. \tag{10}$$

In the EKF, $\mathbf{H}_n$ is linearized based on a first-order Taylor expansion in the neighborhood of the state $\bar{\mathbf{x}}_n$ predicted from the system model:

$$\mathbf{H}_n(\mathbf{x}_n) = \mathbf{H}_n(\bar{\mathbf{x}}_n) + \bar{\mathbf{H}}_n(\mathbf{x}_n - \bar{\mathbf{x}}_n) \tag{11}$$

with the linearized Jacobian matrix

$$\bar{\mathbf{H}}_n = \frac{\partial \mathbf{H}_n(\bar{\mathbf{x}}_n)}{\partial \bar{\mathbf{x}}_n}. \tag{12}$$

Using the linearized matrix, the EKF can be applied in the same way as the linear KF; an update of the state parameters from the actual observation data based on the observation equation and a prediction of the state parameters based on the system model are performed alternately and iteratively at each time step. The predicted state parameter $\mathbf{x}_{n+1}$ is obtained using the estimated state parameter of the previous time step $\hat{\mathbf{x}}_n$ by the system model as shown in the following equation:

$$\bar{\mathbf{x}}_{n+1} = \tilde{\bar{\mathbf{F}}}_n \hat{\mathbf{x}}_n + \mathbf{u}_n. \tag{13}$$

The predicted covariance matrix, $\bar{\mathbf{P}}_{n+1}$, is obtained using the estimated covariance matrix at the previous time step, $\hat{\mathbf{P}}_n$, using the following equation:

$$\bar{\mathbf{P}}_{n+1} = \mathbf{F}_n \hat{\mathbf{P}}_n \mathbf{F}_n^{\mathrm{T}} + \mathbf{Q}_n. \tag{14}$$

The estimated state parameter $\hat{\mathbf{x}}_n$ is obtained using the predicted state parameter $\bar{\mathbf{x}}_n$ using the following equation:

$$\hat{\mathbf{x}}_n = \bar{\mathbf{x}}_n + \mathbf{K}_n\big(\mathbf{y}_n - \mathbf{H}_n(\bar{\mathbf{x}}_n)\big), \tag{15}$$

where $\mathbf{K}_n$ is the Kalman gain, with

$$\mathbf{K}_n = \bar{\mathbf{P}}_n \bar{\mathbf{H}}_n^{\mathrm{T}} \Big(\bar{\mathbf{H}}_n \bar{\mathbf{P}}_n \bar{\mathbf{H}}_n^{\mathrm{T}} + \mathbf{R}_n\Big)^{-1}. \tag{16}$$

The updated covariance matrix is then obtained using the following equation:

$$\hat{\mathbf{P}}_n = \Big(\mathbf{I} + \mathbf{K}_n \tilde{\mathbf{H}}_n\Big) \bar{\mathbf{P}}_n. \tag{17}$$

For the assumption of a laterally stratified sound speed structure, the state vector is defined as

$$\mathbf{x}_n = (\delta \mathbf{p}_n, NTD_n)^{\mathrm{T}} = \Big(\delta p_n^{\mathrm{EW}}, \delta p_n^{\mathrm{NS}}, \delta p_n^{\mathrm{Z}}, NTD_n\Big)^{\mathrm{T}}. \tag{18}$$

We assume the white noise in the stochastic process for the estimation of the array displacement, while we assume the random walk in the stochastic process for estimating NTD. The assumption of the white noise process for estimation of the array displacement is introduced to estimate these parameters in a kinematic manner, independent of time. The assumption of a random walk process for estimation of the NTD is often used for modeling the tropospheric delay in satellite measurements (e.g., Herring et al. 1990). The assumptions are implemented by defining the linear transition matrix, $\mathbf{F}$, as

$$\mathbf{F} = \mathrm{diag}(0, 0, 0, 1) \tag{19}$$

and by defining the process noise matrix as

$$\mathbf{Q}_n = \mathrm{diag}\Big(\sigma_{p^{\mathrm{EW}}}^2, \sigma_{p^{\mathrm{NS}}}^2, \sigma_{p^{\mathrm{Z}}}^2, \Delta t_n \sigma_{\mathrm{NTD}}^2\Big) \tag{20}$$

with

$$\Delta t_n = t_n - t_{n-1}. \tag{21}$$

The variance used in the process noise matrix should be assigned in advance. As explained later in this section, the variance for the NTD, σ_{NTD}^2, is determined by fitting to the observational data. The variance of the array displacements is assumed to be 1.0 m^2 since the array displacements can be estimated even for large abrupt displacements by assigning large values to the variance in the array displacements. Note that, to adjust the average levels of the array displacements using initial array displacements, $\delta \mathbf{p}_0$, we define the control input vector as follows:

$$\mathbf{u}_n \equiv \mathbf{u} = (\delta \mathbf{p}_0, 0)^{\mathrm{T}} = \Big(\delta p_0^{\mathrm{EW}}, \delta p_0^{\mathrm{NS}}, \delta p_0^{\mathrm{Z}}, 0\Big)^{\mathrm{T}}. \tag{22}$$

Unifying Eqs. (18)–(22), the system model [Eqs. (8) and (10)] for the assumption of a laterally stratified sound speed structure is defined. As for the observation model, the observation vector is obtained as

$$\mathbf{y}_n = \left(T_{1,n}^{\mathrm{obs}}, \ldots, T_{k_n,n}^{\mathrm{obs}}\right)^{\mathrm{T}}, \tag{23}$$

where k_n is the total number of the replied seafloor transponders at time, t_n. The non-linear Jacobian matrix is defined as

$$\begin{aligned}\mathrm{H}_n(\mathrm{x}_n) = &\left(T_{1,n}^{\mathrm{cal}}(\delta \mathrm{p}_n) + M(\epsilon_{1,n})NTD_n, \ldots, T_{k_n,n}^{\mathrm{cal}}(\delta \mathrm{p}_n)\right.\\ &\left. + M(\epsilon_{k_n,n})NTD_n\right)^{\mathrm{T}}\end{aligned} \tag{24}$$

and the linearized Jacobian matrix is defined via Eq. (12) as

$$\bar{\mathbf{H}}_n = \begin{pmatrix} \frac{\partial T_{1,n}^{\mathrm{cal}}(\delta\bar{\mathbf{p}}_n)}{\partial \delta p_n^{\mathrm{EW}}} & \frac{\partial T_{1,n}^{\mathrm{cal}}(\delta\bar{\mathbf{p}}_n)}{\partial \delta p_n^{\mathrm{NS}}} & \frac{\partial T_{1,n}^{\mathrm{cal}}(\delta\bar{\mathbf{p}}_n)}{\partial \delta p_n^{\mathrm{Z}}} & M(\epsilon_{1,n}) \\ \vdots & \vdots & \vdots & \vdots \\ \frac{\partial T_{k_n,n}^{\mathrm{cal}}(\delta\bar{\mathbf{p}}_n)}{\partial \delta p_n^{\mathrm{EW}}} & \frac{\partial T_{k_n,n}^{\mathrm{cal}}(\delta\bar{\mathbf{p}}_n)}{\partial \delta p_n^{\mathrm{NS}}} & \frac{\partial T_{k_n,n}^{\mathrm{cal}}(\delta\bar{\mathbf{p}}_n)}{\partial \delta p_n^{\mathrm{Z}}} & M(\epsilon_{k_n,n}) \end{pmatrix}. \tag{25}$$

We assume the same weight among the observed round-trip travel times regardless of the time step as follows:

$$\mathbf{R}_{\mathrm{n}} \equiv \mathbf{R} = \mathrm{diag}\left(\sigma^2, \ldots, \sigma^2\right), \tag{26}$$

where σ^2 corresponds to variance of the measurement errors for the round-trip travel times. Considering that the precision of the acoustic ranging is < ~1 cm (e.g., Fujimoto 2014) and that the precision of the kinematic GNSS positioning on the sea-surface platform is roughly a few centimeters (e.g., Sugimoto et al. 2009), σ^2 is assumed to be 1.0×10^{-9} s^2, which corresponds to an ~5 cm measurement error in the line-of-sight direction.

For the assumption of a horizontally graded sound speed structure, we define the state vectors as

$$\begin{aligned}\mathbf{x}_n &= \left(\delta\mathbf{p}_n, NTD_n, G_n^{\mathrm{EW}}, G_n^{\mathrm{NS}}\right)^{\mathrm{T}} \\ &= \left(\delta p_n^{\mathrm{EW}}, \delta p_n^{\mathrm{NS}}, \delta p_n^{\mathrm{Z}}, NTD_n, G_n^{\mathrm{EW}}, G_n^{\mathrm{NS}}\right)^{\mathrm{T}}.\end{aligned} \tag{27}$$

Similar to the assumptions for a laterally stratified sound speed structure, the array displacements are assumed to be a white noise process, while the NTD is assumed to be a random walk process. Further, the underwater delay gradient is assumed to be a random walk processes, like the tropospheric delay gradients in the satellite measurements (e.g., Bar-Server et al. 1998). Then, as for the system model, the transition matrix and the process noise matrix are defined as follows:

$$\mathbf{F} = \mathrm{diag}(0, 0, 0, 1, 1, 1), \tag{28}$$

$$\mathbf{Q}_n = \mathrm{diag}\left(\sigma_{p^{\mathrm{EW}}}^2, \sigma_{p^{\mathrm{NS}}}^2, \sigma_{p^{\mathrm{Z}}}^2, \Delta t_n \sigma_{\mathrm{NTD}}^2, \Delta t_n \sigma_{G^{\mathrm{EW}}}^2, \Delta t_n \sigma_{G^{\mathrm{NS}}}^2\right). \tag{29}$$

The variance in the array displacements and the NTD is the same as for the case of the laterally stratified sound speed structure. The variance in the underwater delay gradients are determined to fit the observational data, as for that of the NTD. To adjust the average levels of the array displacements using the initial array displacements, $\delta\mathbf{p}_0$, we also define the control input vector as

$$\mathbf{u}_n \equiv \mathbf{u} = (\delta\mathbf{p}_0, 0, 0, 0)^{\mathrm{T}} = \left(\delta p_0^{\mathrm{EW}}, \delta p_0^{\mathrm{NS}}, \delta p_0^{\mathrm{Z}}, 0, 0, 0\right)^{\mathrm{T}}. \tag{30}$$

As for the observation model, the observation vector is obtained using Eq. (23). The kth component of the non-linear Jacobian matrix $\mathbf{H}_n(\mathbf{x}_n)$ is defined as

$$\begin{aligned}H_{k,n}(\mathbf{x}_n) = &\, T_{k,n}^{\mathrm{cal}}(\delta\mathbf{p}_n) + M(\epsilon_{k,n})NTD_n \\ &+ M(\epsilon_{k,n})\cot\epsilon_{k,n}\left(G_n^{\mathrm{EW}}\sin\phi_{k,n} + G_n^{\mathrm{NS}}\cos\phi_{k,n}\right)\end{aligned} \tag{31}$$

and the linearized Jacobian matrix is defined as

$$\bar{\mathbf{H}}_n = \begin{pmatrix} \frac{\partial T_{1,n}^{\mathrm{cal}}(\delta\bar{\mathbf{p}}_n)}{\partial \delta p_n^{\mathrm{EW}}} & \frac{\partial T_{1,n}^{\mathrm{cal}}(\delta\bar{\mathbf{p}}_n)}{\partial \delta p_n^{\mathrm{NS}}} & \frac{\partial T_{1,n}^{\mathrm{cal}}(\delta\bar{\mathbf{p}}_n)}{\partial \delta p_n^{\mathrm{Z}}} & M(\epsilon_{1,n}) & M(\epsilon_{1,n})\cot\epsilon_{1,n}\sin\phi_{1,n} & M(\epsilon_{1,n})\cot\epsilon_{1,n}\cos\phi_{1,n} \\ \vdots & \vdots & \vdots & \vdots & \vdots & \vdots \\ \frac{\partial T_{k_n,n}^{\mathrm{cal}}(\delta\bar{\mathbf{p}}_n)}{\partial \delta p_n^{\mathrm{EW}}} & \frac{\partial T_{k_n,n}^{\mathrm{cal}}(\delta\bar{\mathbf{p}}_n)}{\partial \delta p_n^{\mathrm{NS}}} & \frac{\partial T_{k_n,n}^{\mathrm{cal}}(\delta\bar{\mathbf{p}}_n)}{\partial \delta p_n^{\mathrm{Z}}} & M(\epsilon_{k_n,n}) & M(\epsilon_{k_n,n})\cot\epsilon_{k_n,n}\sin\phi_{k_n,n} & M(\epsilon_{k_n,n})\cot\epsilon_{k_n,n}\cos\phi_{k_n,n} \end{pmatrix}. \tag{32}$$

We also assume the same covariance matrix for the measurement errors using Eq. (26).

The optimal variance for the process noise of the NTD is determined by maximizing likelihood. Given the variance parameter vector as

$$\boldsymbol{\Theta} = \left(\sigma_{\mathrm{NTD}}^2, \sigma_{G^{\mathrm{EW}}}^2, \sigma_{G^{\mathrm{NS}}}^2\right)^{\mathrm{T}} \tag{33}$$

for the case of the horizontally graded SSS (for the case of the laterally stratified SSS, the variance parameter is σ^2_{NTD}, not forming a vector), the log-likelihood is written as follows (e.g., Kitagawa 2005; Segall and Matthews 1997):

$$L(\boldsymbol{\Theta}|\mathbf{y}) = -\frac{1}{2}\left(N\log 2\pi + \sum_{n=1}^{N}\log|\mathbf{V}_n| + \sum_{n=1}^{N}\left(\mathbf{y}_n - \mathbf{H}_n(\mathbf{x}_n)\right)^T\mathbf{V}_n^{-1}\left(\mathbf{y}_n - \mathbf{H}_n(\mathbf{x}_n)\right)\right) \tag{34}$$

with

$$\mathbf{V}_n = \bar{\mathbf{H}}_n\mathbf{P}_n\bar{\mathbf{H}}_n^T + \mathbf{R}_n. \tag{35}$$

Synthetic test

Model setting

To evaluate the performance of the introduced EKF-based array positioning method, we conducted synthetic tests. We analyzed synthetic observational data assuming a horizontally graded SSS with a temporal fluctuation by both the conventional array positioning (e.g., Kido et al. 2006; Kido 2007) method and the EKF-based array positioning method. Note that we performed the above analysis assuming both a laterally stratified SSS and the horizontally graded SSS to investigate how the temporally fluctuating gradient structure affects estimations compared with the case of a laterally stratified SSS. Synthetic round-trip travel-time data were produced based on the observation equation [Eq. (5)] by temporally varying the unknown parameters $\left(\delta\mathbf{p}_n, NTD_n, G_n^{\mathrm{EW}}, G_n^{\mathrm{NS}}\right)$ as follows:

$$\begin{aligned} T_{k,n}^{\mathrm{sys}} = {} & T_{k,n}^{\mathrm{cal}}(\mathbf{p}_k + \delta\mathbf{p}_n; \mathbf{d}_n; v_0) + M\left(\epsilon_{k,n}\right)NTD_n \\ & + M\left(\epsilon_{k,n}\right)\cot\epsilon_{k,n}\left(G_n^{\mathrm{EW}}\sin\phi_{k,n} + G_n^{\mathrm{NS}}\cos\phi_{k,n}\right). \end{aligned} \tag{36}$$

To calculate the synthetic travel-time data, we specified the initial positions of the transponders, $\mathbf{p}_k$, synthetic positions of an acoustic transducer at a sea-surface platform, $\mathbf{d}_n$, and an initial sound speed profile, v_0, as synthetic observational data.

We generated synthetic observational data based on three different geometries for the seafloor transponder array (i.e., the initial positions of the transponders, $\mathbf{p}_k$): four transponders forming a square array geometry (Fig. 2a); six transponders forming a combined large and small triangular array (Fig. 2b); four transponders forming a combined triangular array with an additional transponder at its center (Fig. 2c). The square-formed array geometry is the most popular pattern among the recently established GNSS-A sites in Japan, and the double-triangular array geometry has been adopted at five sites on a trial basis, which provides a multi-angled transponder array (e.g., Kido et al. 2015). The assumed geometries for the square-formed array (Fig. 2a) and for the double-triangular array (Fig. 2b) are same with actual observation sites, the G08 (water depth: 3473 m) and G19 (water depth: 5725 m), located in the off-Tohoku region (Tomita et al. 2017), respectively. The triangular-centered array geometry (Fig. 2c) has not yet been trialed. However, it can be treated as a multi-angled transponder site using only four transponders as illustrated in Fig. 2c; we investigate its performance. Note that we assumed 4000 m of water depth for the synthetic triangular-centered array geometry.

Synthetic positions for an acoustic transducer on a sea-surface platform, $\mathbf{d}_n$, were generated within a radius of 50 m from the array center, imitating a point survey. Note that the actual positions of the sea-surface acoustic transducers were used to calculate the synthetic travel-time data; however, when estimating the unknown parameters in the synthetic tests, we used positions for the sea-surface acoustic transducers contaminated by GNSS positioning errors, with standard deviation of 3 cm for each component. These values where chosen as the precision of the kinematic GNSS positioning on the sea-surface platform is roughly a few centimeters (e.g., Sugimoto et al. 2009).

The initial sound speed profile, v_0, for each site (G08 and G19) was calculated from temperature and salinity data obtained from the World Ocean Atlas 2013 (WOA13; Locarnini et al. 2013; Zweng et al. 2013). WOA13 distributed average underwater structure models for temperature, salinity and other indexes, complied with observational data over the past 60 years. We calculated a temperature and salinity profile for each site and converted them into a sound speed profile following Chen and Millero (1977). The initial sound speed profile for the triangular-centered array geometry is same as that for G17 site also located in the off-Tohoku region, at water depth of 4232 m.

Then we assigned synthetic temporal fluctuations in the unknown parameters. We assumed temporally fixed array displacements for the synthetic tests (all components of the array displacement were fixed to 0.5 m). Note that we provided an initial array displacement of 0.3 m for all components as the control input for Eq. (30) when using the EKF-based array positioning method. Temporal fluctuations in the NTD were expressed as a sine wave with an amplitude of 0.1 ms and a period of 4 h. The east–west component of the temporal fluctuation in the underwater delay gradient, G_n^{EW}, was also expressed as

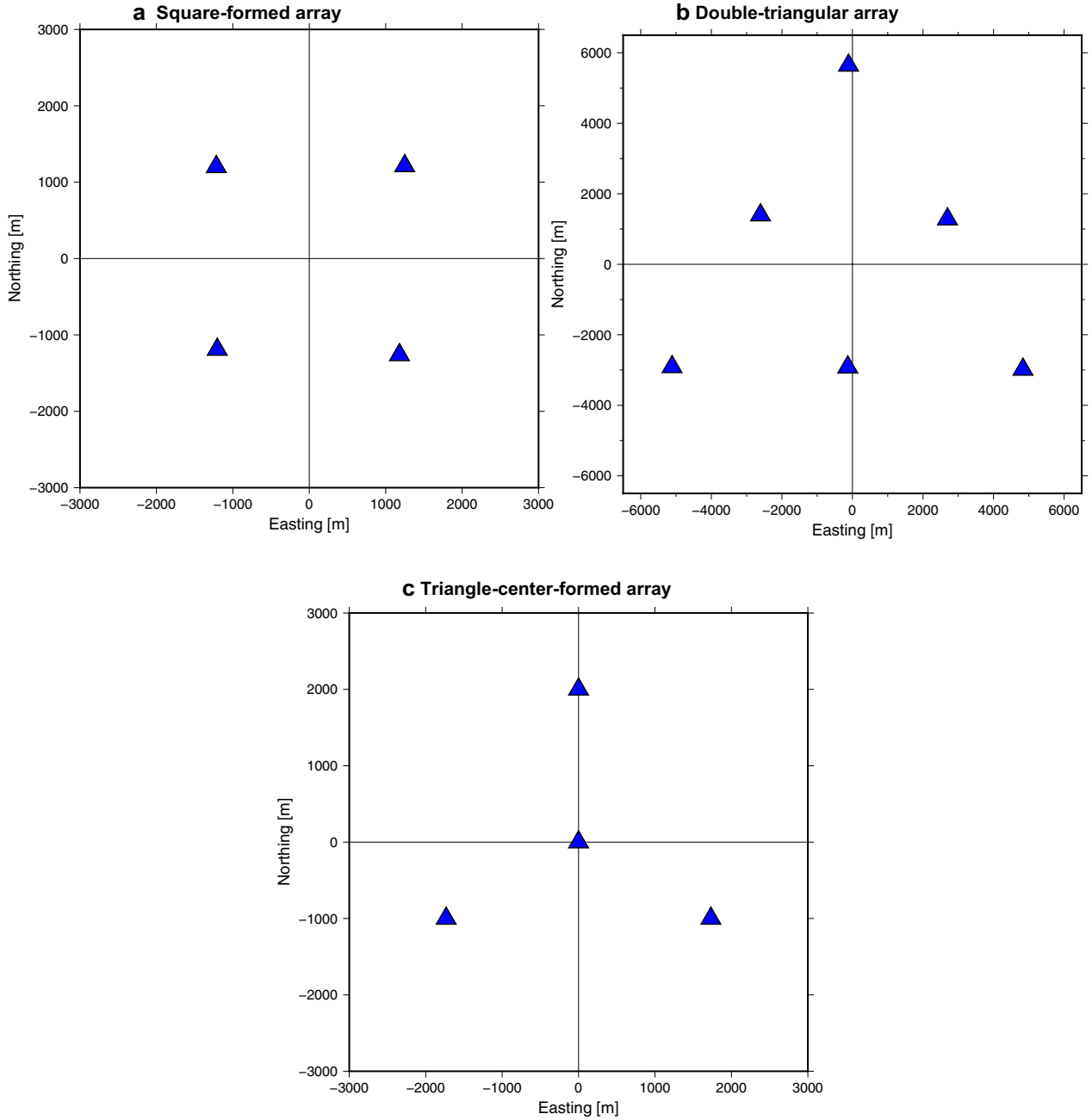

Fig. 2 Array geometries for synthetic tests. **a** A square-formed array geometry at G08 site (depth: 3473 m), **b** a double-triangular array geometry at the G19 site (depth: 5724 m), **c** a triangular-center-formed array geometry at a synthetic site (assumed depth: 4000 m). Blue triangles in each panel represent seafloor transponders

a sine wave with an amplitude of 0.1 ms and a period of 2 h. The north–south component of the underwater delay gradient, G_n^{NS}, was fixed in time.

Based on the above model setup, we calculated the synthetic travel-time data using Eq. (36). In this calculation, a total of 300 shots of the synthetic acoustic pings were sampled at intervals of 60 s. Finally, we added measurement errors to the travel-time data assuming Gaussian noise with a standard deviation of 1.0×10^{-5} s (corresponding to ~0.75 cm in the one-way slant path) since precision of the acoustic ranging is < ~1 cm (e.g., Fujimoto 2014).

Results

Figure 3 shows the kinematic array positioning results for the synthetic data assuming the square-formed array

geometry. The solutions estimated by the conventional array positioning method, which fixed the vertical array displacements to be zero (e.g., Kido et al. 2006, 2008) (black triangles), demonstrated a time-dependent systematic error in the east–west component of the array displacements (Fig. 3a), caused by the prescribed gradient in SSS (Fig. 3e). Since the vertical array displacements are fixed to be zero (Fig. 3c), the estimated NTDs are biased from the true solutions; however, the estimated NTDs could explain the true temporal evolution (Fig. 3d). The solutions obtained by the conventional array positioning method, estimating both vertical and horizontal array displacements, are shown by orange crosses. The estimated vertical array displacements are out of plotting range in Fig. 3c, with displacements of up to $\pm\sim 10$ m. As the estimated NTDs are also out of plotting range in Fig. 3d, the trade-off relationship between the vertical array displacements and the NTDs cannot be solved in the square-formed array geometry when only conducting a point survey. Further, the unsolved NTDs might degrade the precision of the horizontal array displacements (Fig. 3a, b). The EKF-based array positioning, assuming a laterally stratified SSS (blue squares), prevents the vertical array displacements and the NTDs from diverging. However, the trade-off cannot be solved even when using the EKF-based array positioning, meaning that the vertical array displacements and the NTDs deviated from the true values over time. The horizontal components of the array displacements are almost the same as the solutions obtained from the conventional array positioning method with fixed vertical array displacements (Fig. 3a, b) since the NTDs did not diverge through the EKF-based array positioning in this time window. Estimation results of the EKF-based array positioning assuming a horizontally graded SSS (purple circles) showed similar vertical array displacements and NTDs to predictions assuming a laterally stratified SSS (Fig. 3c, d). In the EKF-based array positioning, the horizontal components of the array displacements also deviated from the true values with time because of the

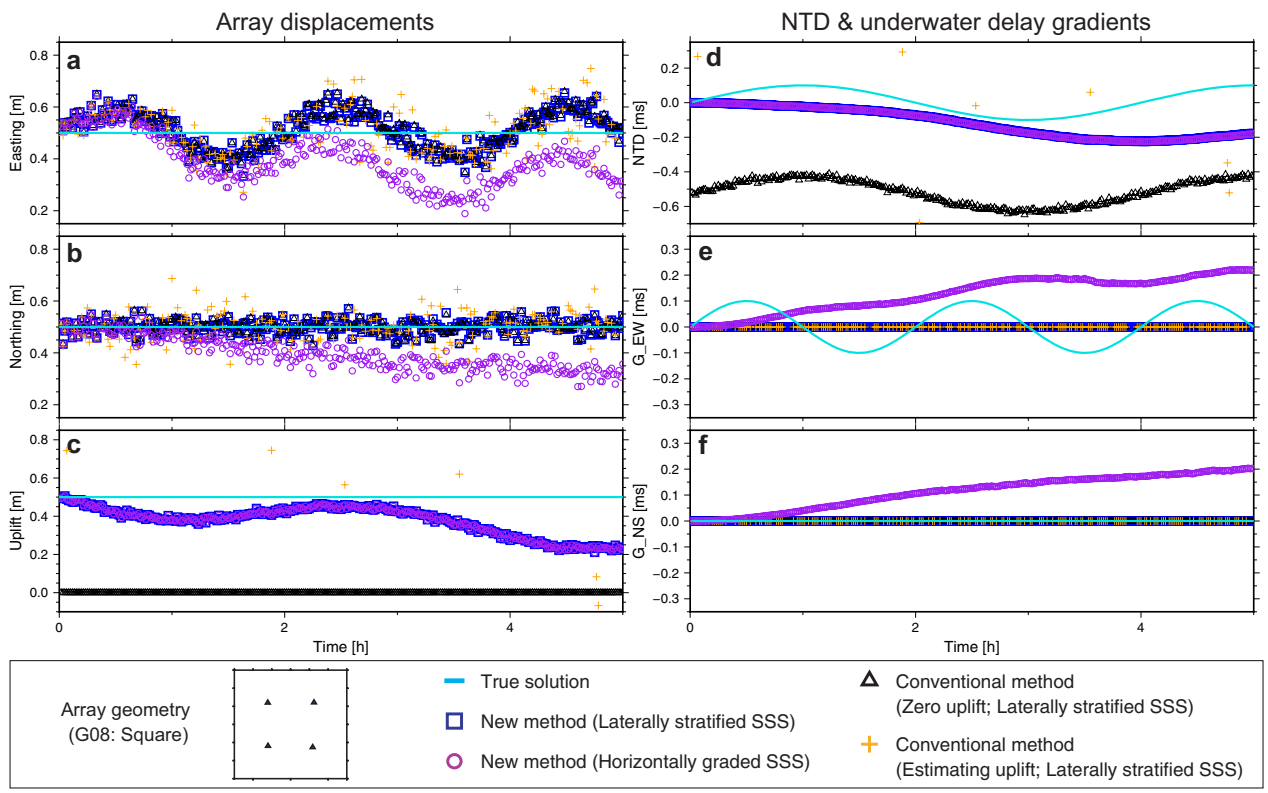

Fig. 3 Synthetic test results assuming the square-formed array geometry. Kinematic array positioning results of the synthetic data assuming the square-formed array geometry (Fig. 2a) are shown: **a** east–west component of array positions, **b** north–south component of array positions, **c** vertical component of array positions, **d** NTD, **e** east–west component of underwater delay gradient, and **f** north–west component of underwater delay gradient. Cyan curves represent the true values for the synthetic data. Black triangles, orange crosses, blue squares, and purple circles show the results estimated by conventional array positioning fixing the vertical component, conventional array positioning solving the vertical component, EKF-based array positioning assuming a laterally stratified sound speed structure, and EKF-based array positioning assuming a horizontally graded sound speed structure, respectively

trade-off relationship between the array displacements and the underwater delay gradients (Fig. 3a, b).

Figure 4 shows the kinematic array positioning results for the synthetic data assuming the double-triangle array geometry. The conventional array positioning method of fixed zero vertical array displacements showed similar results to the case of the square-formed array geometry (black triangles in Fig. 4a–l), but for this new geometry, the conventional array positioning method was also able to resolve the vertical array displacements and the NTDs (orange crosses in Fig. 4a–f). This improvement is a result of the multi-angled transponders solving the vertical array displacements with the NTDs as explained in "The observation equation analogy to satellite measurements". Furthermore, the EKF-based array positioning method, assuming the laterally stratified SSS, further demonstrates the superior performance for the vertical array displacements (blue squares in Fig. 4c) since the EKF provides a temporal constraint on NTDs that avoids numerical instability when solving the vertical array displacements and NTDs. The conventional array positioning method [an updated method from Kido (2007) based on Eq. (5)] and the EKF-based array positioning method for the horizontally graded SSS are shown in Fig. 4g–l as green diamonds and purple circles, respectively. The conventional method approximately solves the gradient parameters (Fig. 4k, l), but the solutions of the gradient parameters and of the horizontal array displacements have large dispersions, probably because of the potential trade-off relationship among them. Meanwhile, the EKF-based array positioning method stably solves those parameters by constraining the temporal evolution of the gradient parameters and greatly reduces the dispersion in the horizontal array displacements.

Figure 5 shows the kinematic array positioning results for the synthetic data assuming the triangular-centered array geometry. The conventional array positioning method can resolve the vertical array displacements and the NTDs unlike for the case of the square-formed array geometry (orange crosses in Fig. 5c, d). However, note that the dispersion of the vertical array displacements is a little larger that the case of the double-triangular-formed array geometry probably because of insufficient variation in the shot angles. The EKF-based array positioning method can improve the precision of the vertical array displacements (blue squares in Fig. 5c) by temporally constraining NTDs similar to the double-triangular-formed array geometry. Although the underwater delay gradients cannot be solved in the case of the triangular-centered array geometry (Fig. 5e, f), this geometry enables us to detect kinematic vertical array displacements accurately, using only four transponders (the double-triangular-formed array geometry requires six transponders). Furthermore, the precision of the vertical array displacements can be improved using the EKF-based array positioning method, assuming a laterally stratified SSS.

Through the synthetic test, we confirmed (1) the utility of the multi-angled transponders for detecting the kinematic vertical array displacements, (2) the accurate performance of the EKF-based array positioning method for precisely detecting the vertical array displacements at the multi-angled transponder sites, and (3) the accurate kinematic solutions to the underwater delay gradients for the double-triangular-formed array geometry site via the EKF-based array positioning method.

Point (1) shows the importance of acoustic data with various shot angles during a point survey. Effects of a temporal sound speed fluctuation can be expressed by NTDs that are independent of shot angles, whereas the vertical array displacement is sensitive to variation of shot angles. We validated this fact through a simple numerical test. We assumed a two-dimensional field as shown by Fig. 6a, and five transponders are vertically located. When perturbation is given in the average sound speed, the one-way travel-time residual can be expressed as follows:

$$\delta T(\delta v) = T(v_0 + \delta v) - T(v_0) = \sqrt{x^2 + d_0^2}\left(\frac{1}{v_0 + \delta v} - \frac{1}{v_0}\right). \tag{37}$$

Using the mapping function, contribution of the sound speed perturbation to the travel-time residual is common with each transponder. In other words, the travel-time residual normalized by the mapping function is independent of the horizontal distance of the transducer (i.e., shot angle) as follows:

$$\delta T^{\text{normlized}}(\delta v) = \delta T(\delta v)/M(\epsilon) = d_0\left(\frac{1}{v_0 + \delta v} - \frac{1}{v_0}\right). \tag{38}$$

Figure 6b shows the normalized travel-time residuals when various values of the sound speed perturbation are given. Figure 6b clearly demonstrates that the normalized travel-time residuals are same among the transducers. Meanwhile, when perturbation in depth is given, the travel-time residual can be written as follows:

$$\begin{aligned}\delta T(\delta d) &= T(d_0 + \delta d) - T(d_0) \\ &= \frac{1}{v_0}\left(\sqrt{x^2 + (d_0 + \delta d)^2} - \sqrt{x^2 + d_0^2}\right).\end{aligned} \tag{39}$$

Then the normalized travel time can be also written as follows:

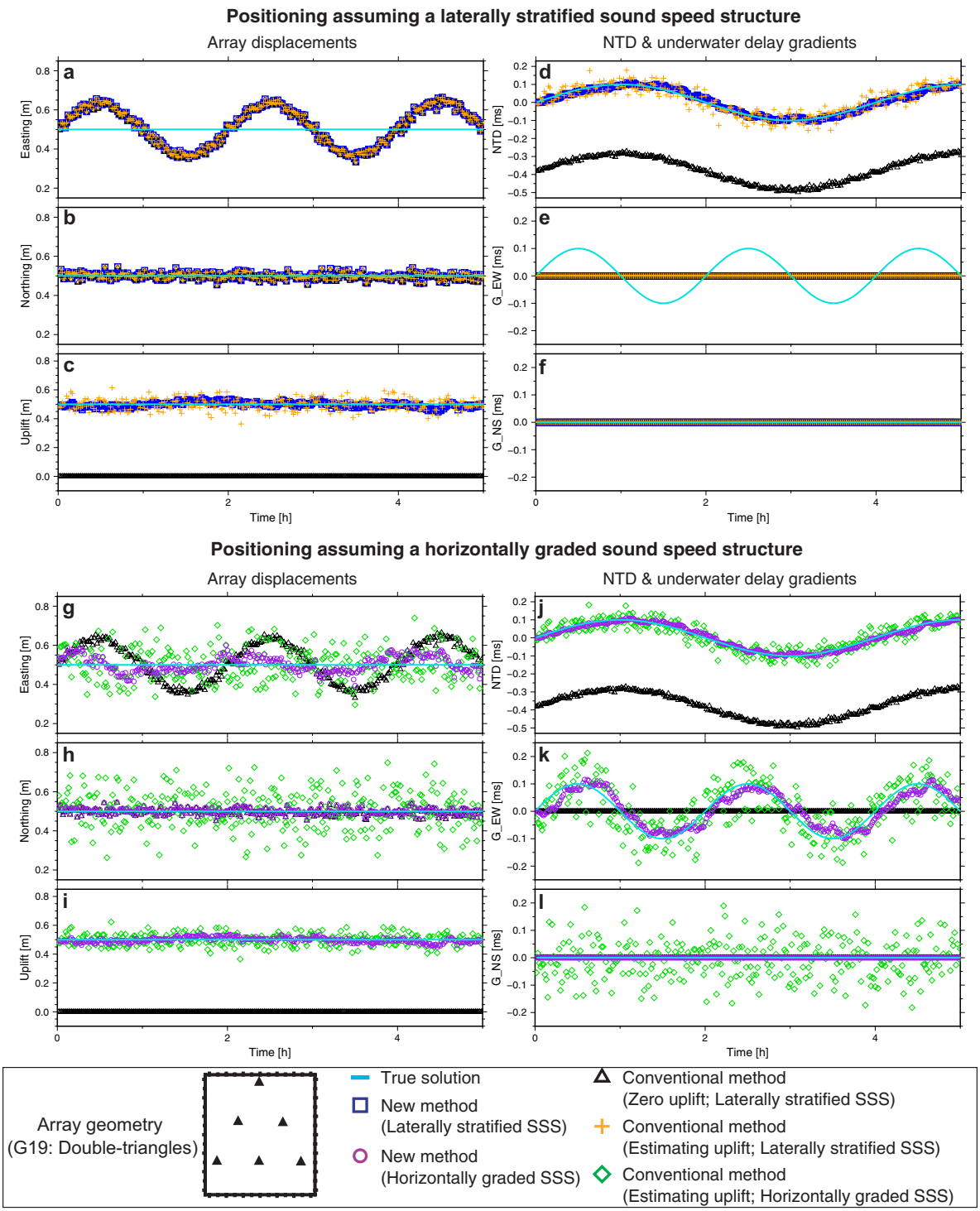

Fig. 4 Synthetic test results assuming the double-triangular array geometry. Kinematic array positioning results of the synthetic data assuming the double-triangular array geometry (Fig. 2b) are shown: **a**, **g** east–west component of array positions, **b**, **h** north–south component of array positions, **c**, **i** vertical component of array positions, **d**, **j** NTD, **e**, **k** east–west component of underwater delay gradient, and **f**, **l** north–west component of underwater delay gradient. **a**–**f** Positioning results assuming a laterally stratified sound speed structure; **g**–**l** positioning results assuming a horizontally graded sound speed structure. Green diamonds show the results estimated by conventional array positioning solving the vertical component assuming a horizontally graded sound speed structure, and other symbols shown are the same as in Fig. 3

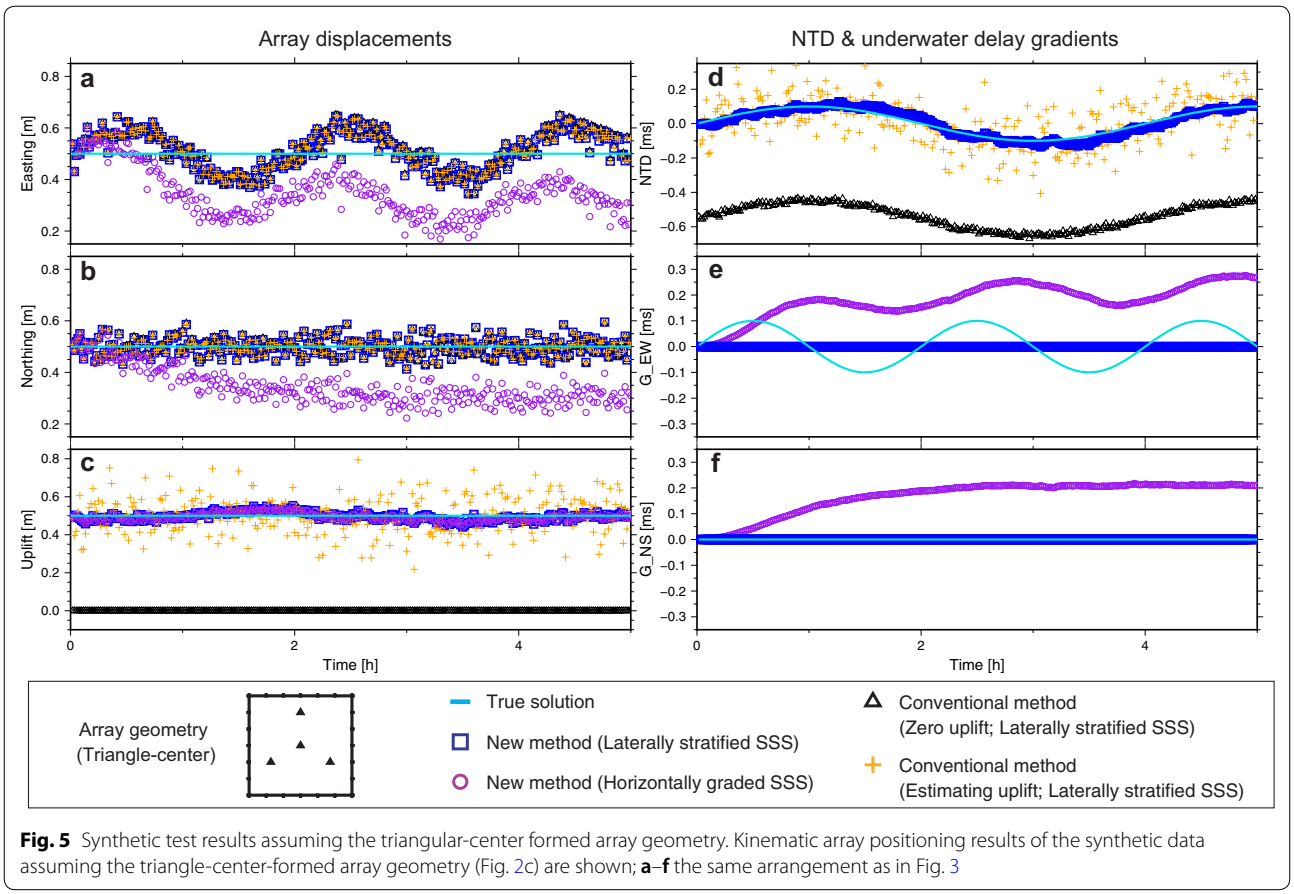

Fig. 5 Synthetic test results assuming the triangular-center formed array geometry. Kinematic array positioning results of the synthetic data assuming the triangle-center-formed array geometry (Fig. 2c) are shown; **a**–**f** the same arrangement as in Fig. 3

$$\delta T^{\mathrm{normlized}}(\delta d) = \delta T(\delta d)/M(\epsilon) = \frac{d_0}{\nu_0}\left(\frac{\sqrt{x^2+(d_0+\delta d)^2}}{\sqrt{x^2+d_0^2}} - 1\right). \tag{40}$$

Figure 6c shows the normalized travel-time residuals when various values of the perturbation in depth are given. Figure 6c demonstrates that the normalized travel-time residuals vary depending on the absolute horizontal distance from the array center (i.e., absolute shot angles). This indicates that if the absolute shot angles for the transponders from the array center are same (such as the square-formed array geometry), we cannot distinguish contributions of the sound speed perturbation from those of the depth perturbation. Thus, variation in absolute shot angles is essential to precisely estimate vertical displacements in the kinematic GNSS-A positioning.

In the next section, we apply the EKF-based array positioning methods to actual observational data.

Application

Actual observation data

We used the actual GNSS-A observational data collected by Tomita et al. (2017) in the off-Tohoku region. We used the observational data collected on March 14, 2015, at the G08 site (longitude: 143.647°E, latitude: 38.721°N, depth: 3473 m) as an example of the square-formed array geometry (Fig. 7). Moreover, we used the observational data collected on February 28, 2015, at the G19 site (longitude: 142.671°E, latitude: 36.496°N, depth: 5725 m) as an example of the double-triangular-formed array geometry (Fig. 8). The details of the observational data are shown in Tomita et al. (2017).

For GNSS positioning using the KF, the process noises are often assigned as fixed values (e.g., Bar-Server et al. 1998; Hirata and Ohta 2016) because there is high computational cost to determine the optimal process noise values. Therefore, it is worthwhile to search for "general" process noise values to use with the EKF-based GNSS-A array positioning method. From the synthetic tests, we have found that the double-triangular-formed array geometry is suitable for the EKF-based array positioning method, regardless of the assumed SSS. Therefore,

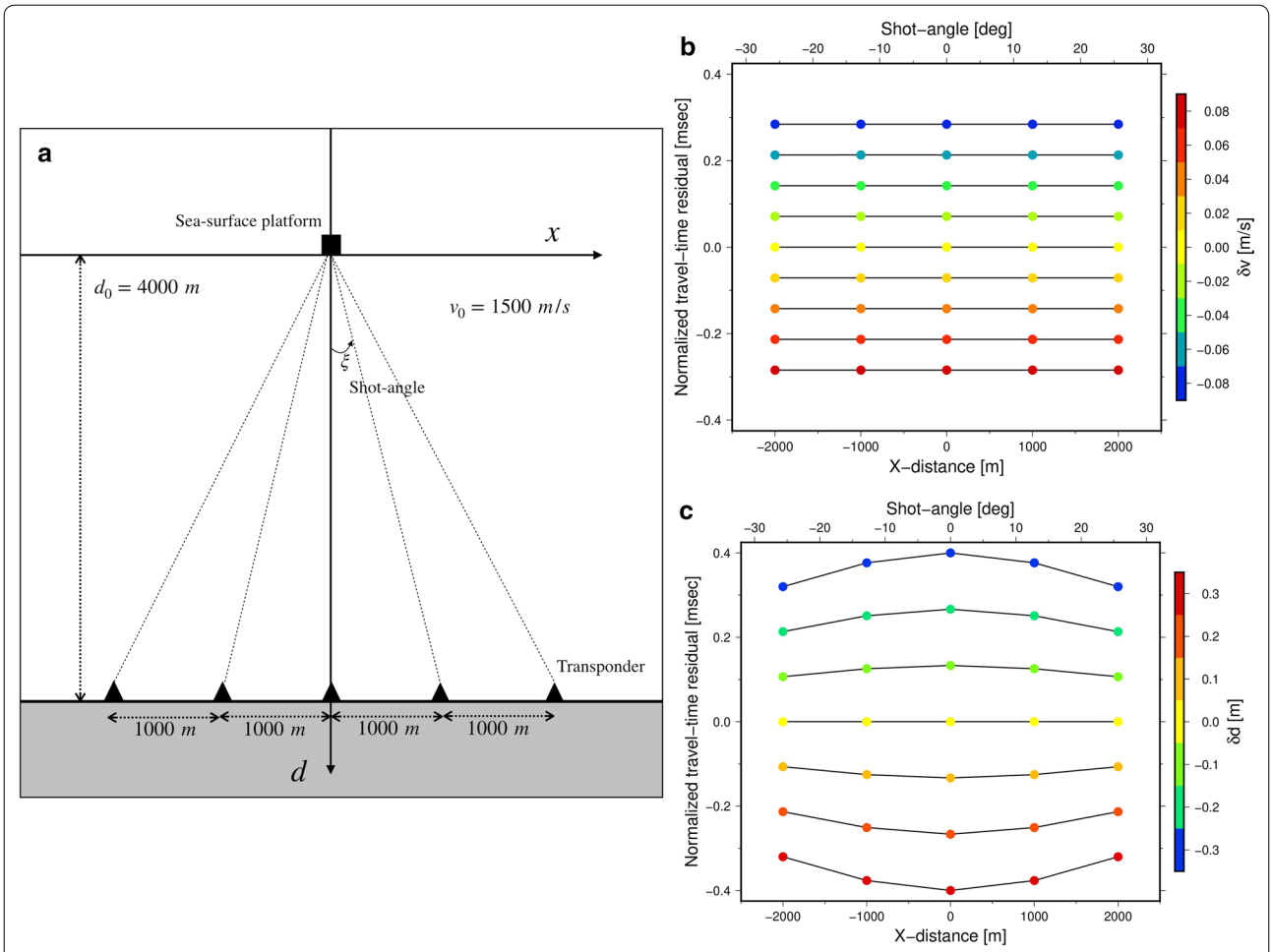

Fig. 6 Numerical test for sensitivity of the normalized travel-time residual to the sound speed and to the vertical displacement. **a** Schematic image for the numerical test. Five seafloor transponders located along the horizontal axis, and the sea-surface platform located at the horizontal distance of zero. **b** The normalized travel-time residual for each transponder given a perturbation in the average sound speed. The color shows the perturbation in the average sound speed. **c** The normalized travel-time residual for each transponder given a perturbation in the vertical displacement. The color shows the perturbation in the vertical displacement

we investigated the optimal process noise values by maximizing the likelihood of the actual observational data, at sites with the double-triangular-formed array geometry. Thus, we also analyzed all the observational data at the sites forming the double-triangular-formed array geometry collected by Tomita et al. (2017): G04 (longitude: 143.897°E, latitude: 39.566°N, depth: 4587 m), G10 (longitude: 143.483°E, latitude: 38.302°N, depth: 3271 m), G15 (longitude: 143.521°E, latitude: 37.677°N, depth: 5264 m) and G19 sites. Then we compared the determined process noise values.

Results

Figure 7 shows the kinematic array positioning results for the actual observational data at the G08 site (the square-formed array geometry). We analyzed the observational data using the conventional array positioning method of fixed vertical array displacements (black triangles), the conventional array positioning method estimating the vertical array displacements as well as the horizontal array displacements (orange crosses), and the EKF-based array positioning method assuming a laterally stratified SSS (blue squares). The general features of the positioning results are similar to the synthetic test results, assuming the square-formed array geometry (Fig. 3); the vertical array displacements could not be solved due to the trade-off relationship between the vertical array displacements and the NTDs, even by the EKF-based array positioning method, and the horizontal array displacements estimated by the EKF-based array positioning method were almost the same with those estimated by the conventional array positioning method of fixed vertical array displacements.

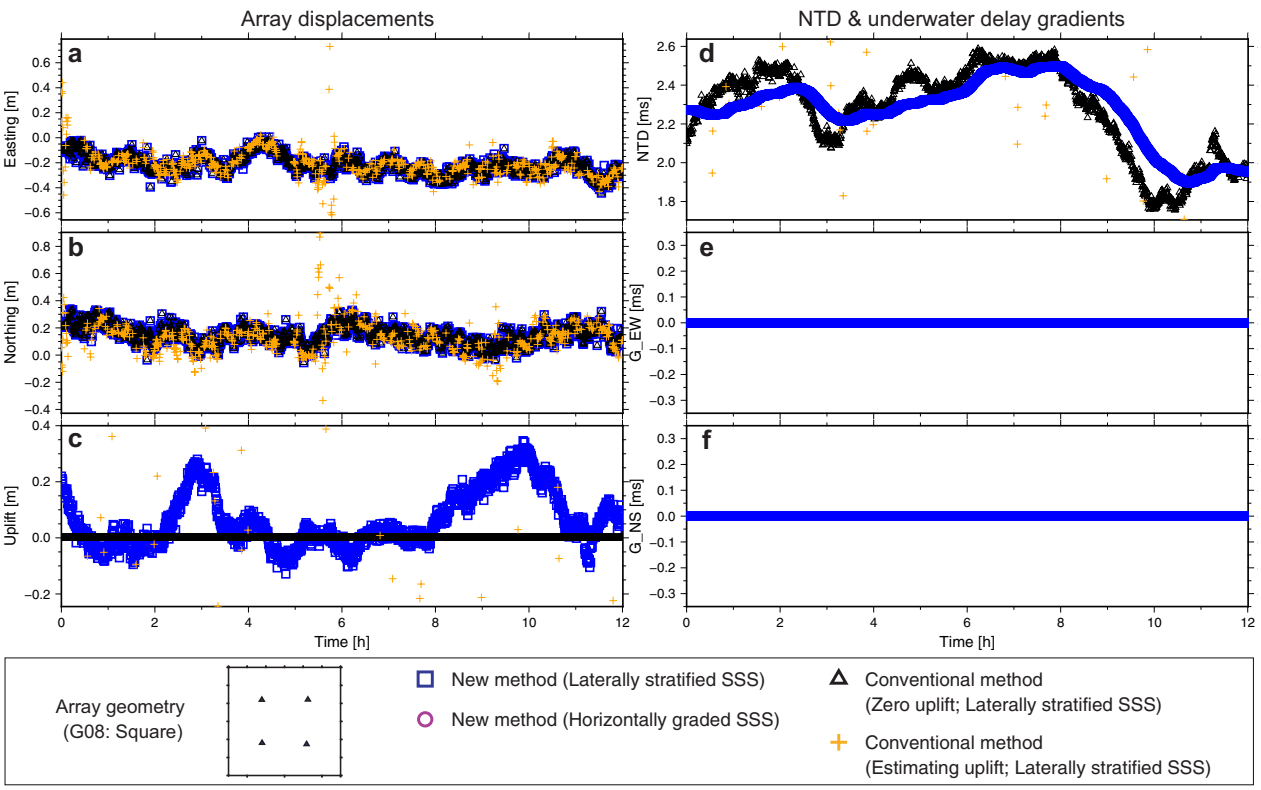

Fig. 7 Positioning results for the actual observational data at G08. Kinematic array positioning results of the actual observational data at site G08, which were obtained during the cruise conducted in February–March 2015 are shown; **a**–**f** the same arrangement as in Fig. 3. The horizontal axis represents time from 15:17:16 on March 14, 2015 (UTC). Colored symbols are the same as shown in Fig. 3

Figure 8a–f shows the kinematic array positioning results for the actual observational data at the G19 site (the double-triangular-formed array geometry) analyzed using the positioning method assuming a laterally stratified SSS. The general features of these positioning results are similar to those of the synthetic test for the double-triangular-formed array geometry (Fig. 4a–f); the horizontal components of the solutions estimated by this method are roughly in accordance. The vertical array displacements can be determined using the conventional array positioning method of estimated vertical array displacements (orange crosses) and the EKF-based array positioning method (blue squares). Moreover, the EKF-based array positioning method can detect the vertical array displacements more precisely than the conventional array positioning method. Although the horizontal array displacements estimated by the conventional array positioning method of fixed vertical displacements agree well with those estimated using the EKF-based array positioning method in the synthetic test (Fig. 4a, b), they sometimes disagree for the actual observational data (black triangles in Fig. 8a, b). The causes of this are discussed later in "Robustness in the case of an unresponsive transponder". Unlike the synthetic test, the vertical array displacements estimated using the EKF-based array positioning method fluctuate with time, and the fluctuation is up to a few tens of centimeters, although the vertical array displacements should be constant during the cruise; the causes of this are discussed later in "Improvements to detection of vertical array displacements".

Features of the positioning results for the actual observational data at the G19 site, analyzed using the positioning methods assuming a horizontally graded SSS (Fig. 8g–l), are quite different from the results of the synthetic test (Fig. 4g–l). The horizontal components of the solutions showed large fluctuations with time in both cases of the conventional array positioning method (green diamonds) and of the EKF-based array positioning method (purple circles). The variations are larger than those observed from the solutions obtained assuming a laterally stratified SSS. These variations show short-term (~a few hours) periodic fluctuations (non-random variations); the degraded positioning results are attributed to systematic modeling errors in the underwater delay gradients. These modeling errors are discussed later in "Sound speed structure in actual ocean". Meanwhile,

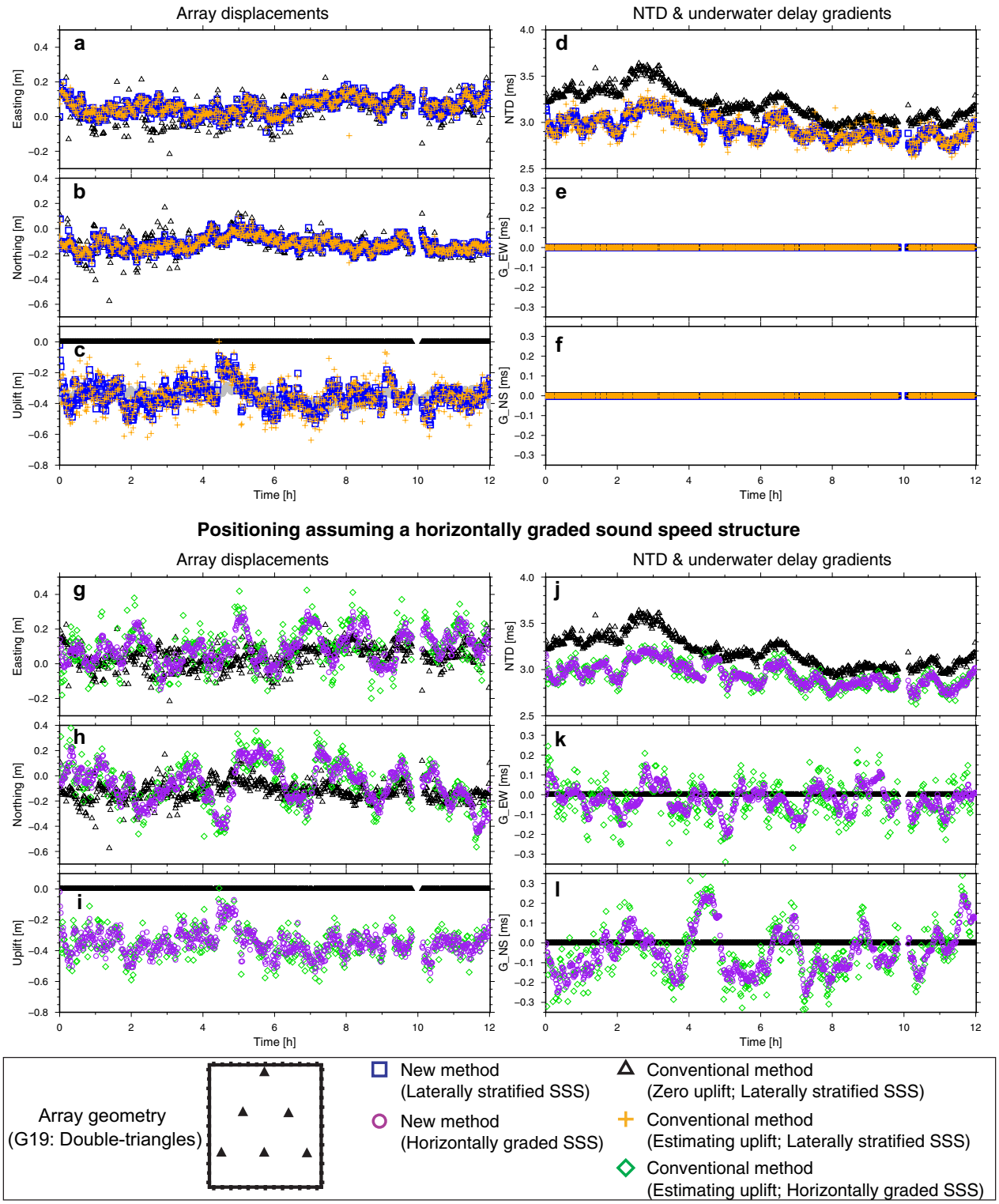

Fig. 8 Positioning results for the actual observational data at site G19. Kinematic array positioning results of the actual observation data at site G19, which were obtained during the cruise conduced in February–March 2015 are shown; **a**–**l** the same arrangement as in Fig. 4. The horizontal axis represents time from 03:04:16 on February 28, 2015 (UTC). The gray bold curve in **c** shows the vertical position changes of the acoustic transducer on the sea-surface platform eliminating geoid height and tidal motions; the average level of the vertical positions is adjusted for comparison with the vertical array displacements. The other colored symbols are the same as those presented in Fig. 4

Table 1 Estimated process noise values using actual data at G04, G10, G15 and G19

Site name	Date	Laterally stratified SSS ($s/s^{1/2}$)	Horizontally gradient SSS ($s/s^{1/2}$)		
		σ_NTD	σ_NTD	σ_G(EW)	σ_G(NS)
G04	September 22, 2012	2.07×10^{-3}	2.06×10^{-3}	1.87×10^{-3}	2.10×10^{-3}
G04	August 12, 2013	2.05×10^{-3}	1.79×10^{-3}	1.77×10^{-3}	1.69×10^{-3}
G04	November 4, 2013	1.61×10^{-3}	1.61×10^{-3}	2.05×10^{-3}	2.17×10^{-3}
G04	March 7, 2015	1.73×10^{-3}	1.74×10^{-3}	1.35×10^{-3}	1.41×10^{-3}
G04	November 3, 2015	1.50×10^{-3}	1.50×10^{-3}	1.59×10^{-3}	1.88×10^{-3}
G04	May 14, 2016	2.66×10^{-3}	2.58×10^{-3}	1.91×10^{-3}	2.08×10^{-3}
G10	September 13, 2012	1.85×10^{-3}	1.87×10^{-3}	2.15×10^{-3}	1.72×10^{-3}
G10	November 29, 2012	2.98×10^{-3}	2.42×10^{-3}	2.19×10^{-3}	1.86×10^{-3}
G10	July 29, 2013	2.04×10^{-3}	1.62×10^{-3}	1.81×10^{-3}	1.66×10^{-3}
G10	March 4, 2014	2.37×10^{-3}	2.28×10^{-3}	2.22×10^{-3}	2.48×10^{-3}
G10	September 20, 2014	1.69×10^{-3}	1.67×10^{-3}	1.74×10^{-3}	1.74×10^{-3}
G10	November 20, 2015	1.77×10^{-3}	1.74×10^{-3}	2.33×10^{-3}	2.41E−03
G10	May 20, 2016	2.11×10^{-3}	2.02×10^{-3}	2.42×10^{-3}	2.18×10^{-3}
G15	March 1, 2014	1.88×10^{-3}	1.85×10^{-3}	1.67×10^{-3}	1.42×10^{-3}
G15	November 9, 2015	1.81×10^{-3}	1.67×10^{-3}	2.11×10^{-3}	1.94×10^{-3}
G15	May 7, 2016	1.85×10^{-3}	1.57×10^{-3}	1.85×10^{-3}	1.63×10^{-3}
G19	September 6, 2012	2.33×10^{-3}	2.09×10^{-3}	2.19×10^{-3}	2.26×10^{-3}
G19	July 25, 2013	2.05×10^{-3}	1.86×10^{-3}	1.97×10^{-3}	1.82×10^{-3}
G19	February 26, 2014	3.01×10^{-3}	3.00×10^{-3}	1.80×10^{-3}	1.71×10^{-3}
G19	February 28, 2015	2.05×10^{-3}	1.99×10^{-3}	1.62×10^{-3}	1.82×10^{-3}
G19	November 15, 2015	2.19×10^{-3}	2.14×10^{-3}	2.15×10^{-3}	1.90×10^{-3}
G19	May 2, 2016	1.70×10^{-3}	1.65×10^{-3}	1.68×10^{-3}	1.89×10^{-3}
Average		2.06×10^{-3}	1.94×10^{-3}	1.93×10^{-3}	1.90×10^{-3}
Standard deviation		0.40×10^{-3}	0.36×10^{-3}	0.26×10^{-3}	0.28×10^{-3}

The estimated process noise values are shown, and their units are all $s/s^{1/2}$. The process noise values for NTD are shown in the both cases of the laterally stratified SSS (column 3) and the horizontally gradient SSS (column 4). The process noise values for underwater delay gradients in east–west and north–south components are shown in the case of horizontal gradient SSS (columns 5 and 6, respectively)

the estimated vertical array displacements and NTDs are almost the same as the solutions obtained assuming a laterally stratified SSS. Thus, the NTDs can be solved independently of the crucial modeling errors in the underwater delay gradients. Additional file 1: Figures S4–S8 show positioning results at the G19 site for the actual observational data collected from the other cruises, and the features of the positioning results mentioned above are also found in the results of other cruises.

The process noise values determined from the actual observational data, for the double-triangular-formed array geometry, are summarized in Table 1. The optimal process noise values (σ_{NTD}) are determined to be $\sim 2.0 \times 10^{-3}$ ($s/s^{1/2}$) regardless of the assumed SSS, the observation site and the observation period. Thus, this value would be generally applicable. Although the process noise values of the underwater delay gradient were determined to be $\sim 1.9 \times 10^{-3}$ ($s/s^{1/2}$) in both the east–west and north–south components ($\sigma_{G^{\mathrm{EW}}}$, $\sigma_{G^{\mathrm{NS}}}$), these values are not reliable because the estimated horizontal array displacements assuming a horizontally graded SSS were not accurately determined, as explained above.

Discussion

Performance of the EKF-based array positioning method

Here, we discuss the utility of our newly developed EKF-based array positioning method. As shown in "Results", the EKF-based array positioning method, assuming a laterally stratified SSS, shows superior performance when compared to the conventional array positioning methods. The advantages of the EKF-based array positioning method are (1) robust positioning accuracy even when some seafloor transponders are unresponsive; (2) precise detection of the vertical array displacements; (3) applicability to continuous GNSS-A positioning. These advantages are discussed in this section. However, in instances of a horizontally graded SSS, the EKF-based array positioning method failed to improve on the precision of the array positioning results, when compared to

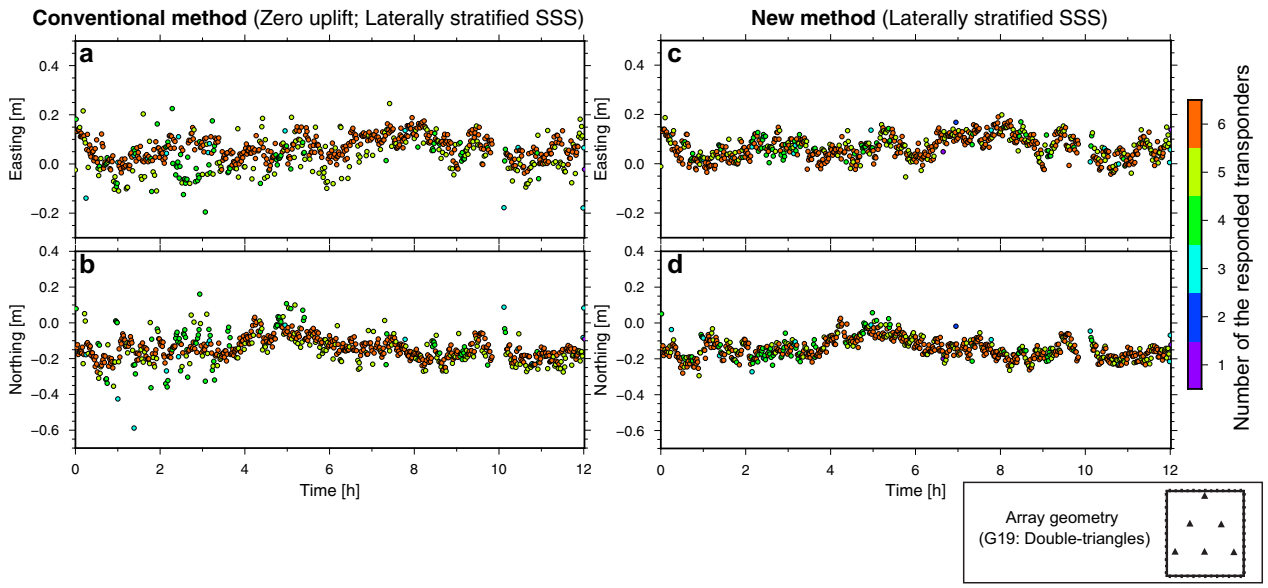

Fig. 9 Horizontal array displacements for the actual data at site G19. Horizontal array displacements estimated by the conventional array positioning method with fixed vertical array displacements are shown as black inverse triangles in Fig. 7a, b and are re-shown as colored dots in **a** and **b** for the east–west and the north–south components, respectively. Horizontal array displacements estimated by the EKF-based array positioning method assuming a laterally stratified SSS, shown as blue squares in Fig. 7a, b, and re-shown as colored dots in **c** and **d** for the east–west and the north–south components, respectively. The colors represent the number of the responsive seafloor transponders at the corresponding acoustic ping

other methods. The causes of this failure are discussed in "Sound speed structure in actual ocean".

Robustness in the case of an unresponsive transponder

The horizontal array displacements for the actual observational data estimated using the conventional array positioning method with fixed vertical array displacements (black triangles in Fig. 8a, b) show little scatter when compared with those estimated using the conventional and the EKF-based array positioning methods. Figure 9a, b also shows the horizontal array displacements for the same data estimated using the conventional array positioning method of fixed vertical array displacements, and the plotted color represents the number of the responding transponders for each ping. This illustrates that the scattered array displacements appear when some transponders are not responding. Such response failures can arise for various reasons including, for example, significant background mechanical noise, bad weather and overlaps in the signal response. For examples, in the observational data obtained in March 2015 at G19 (Fig. 8), three transponders configuring the inner triangle well responded (data acquisition ratio is ~97 percent), while the other three transponders configuring the outer triangle occasionally failed to responded (data acquisition ratio is ~83 percent). Yet in the observational data obtained in November 2015 at G19 (Additional file 1: Figure S7), all transponders well responded (data acquisition ratio is ~97 percent).

To investigate the influence of the unresponsive transponders, we performed additional synthetic test with intermittent transponder failures (Fig. 10). The conditions of these synthetic test are similar to those assuming the double-triangular-formed array geometry, but the temporal fluctuations in the underwater delay gradients are omitted (thus, the horizontal array displacements should be constant with time). In the test, 40% of the responses from the transponders are randomly excluded. Figure 10a–c shows the array displacements estimated using the kinematic array positioning method (true array displacements are 0.5 m for all components). As seen for the actual observational data (Fig. 8), the conventional (orange crosses) and the EKF-based (colored dots) methods estimating the vertical array displacements generally detect true horizontal array displacements, whereas the conventional array positioning method of fixed vertical array displacements (black triangles) provides scattered solutions. However, assuming that the true vertical array displacements are zero, the conventional array positioning method with fixed vertical array displacements successfully provides comparable horizontal array displacements (black triangles in Fig. 10d–e; note that they are totally overlapped with the colored dots). These synthetic tests suggest that deviation of the vertical array

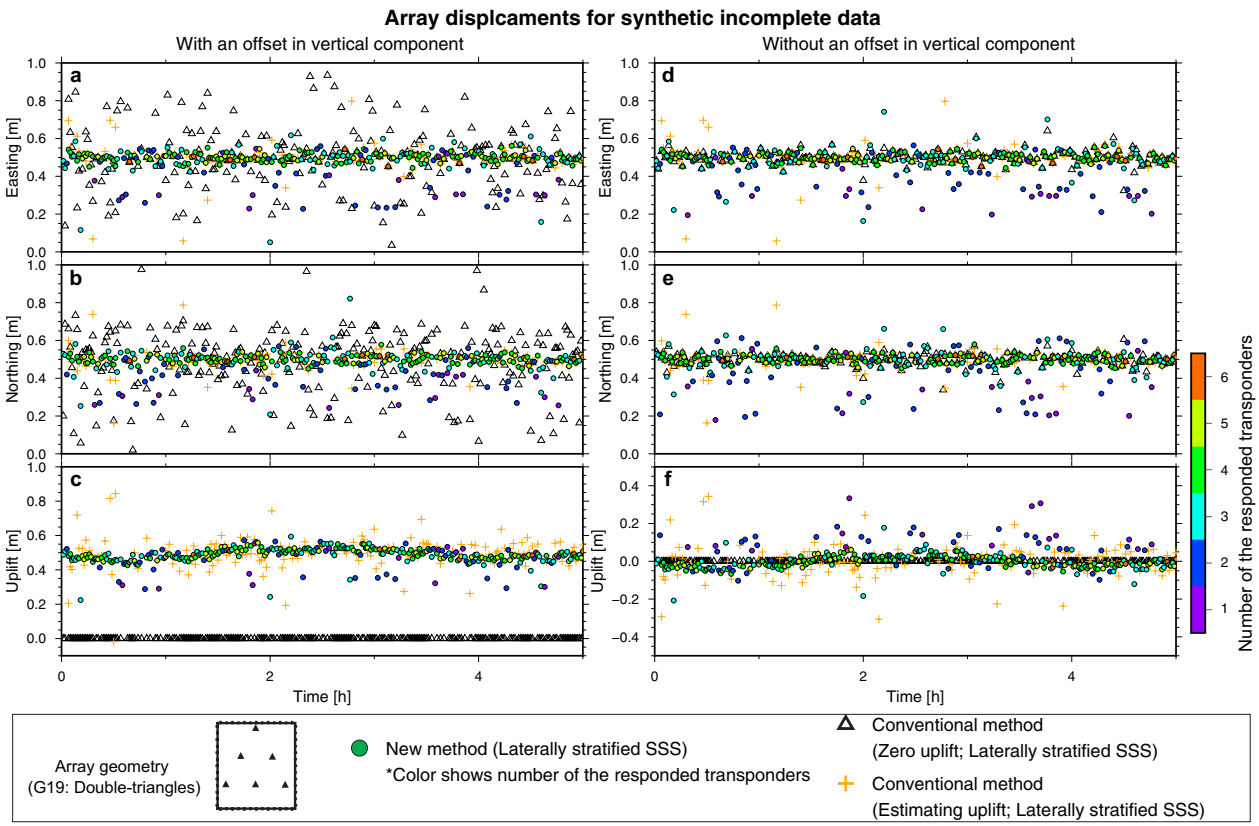

Fig. 10 Positioning results for the synthetic data at site G19 considering unresponsive transponders. Array positioning results for the synthetic data at G19 are shown. The synthetic data for **a**–**c** assume a vertical array displacement of 0.5 m, while those for **d**–**f** assume the vertical array displacements are zero. Black triangles show the solutions for the conventional array positioning method, fixing the vertical array displacements, and orange crosses show the solutions for the conventional array positioning method estimating the vertical array displacements. Colored dots show the solutions for the EKF-based array positioning method assuming a laterally stratified SSS, and the colors represent the number of responsive seafloor transponders at the corresponding acoustic ping

displacements from true values would produce crucial modeling errors in the horizontal array displacements when some transponders fail to respond. We considered that this modeling error is related to the apparent shift in the point of the array center when some transponders fail to respond. Since the accuracy of the array positioning degrades away from the array center (e.g., Kido 2007; Imano et al. 2015, 2019), deviation of the vertical array displacements results in serious modeling errors due to the apparent shift in the point of the array center. This problem can be avoided by estimating the vertical array positions precisely. Since the precision of the vertical array displacements estimated using the EKF-based array positioning method is better than that of the conventional array positioning method, the EKF-based array positioning method can stably perform the array positioning not only for the vertical array displacements but also for the horizontal array displacements, as shown from the analyses of the actual observational data (e.g., Fig. 8a–c; Additional file 1: Figure S8a–c).

Figure 10 further illustrates the robustness of the EKF-based array positioning method in the instance of unresponsive transponders. In principle, the EKF-based array positioning method can estimate the unknown parameters even when the number of observations is smaller than the number of unknown parameters. The colors of the dots (the solutions from the EKF-based array positioning method) in Fig. 10 represent the number of unresponsive transponders; the EKF-based array positioning method can provide accurate solutions when more than three responsive transponders are available. When less than two responsive transponders are available, the array positions are estimated to be 0.3 m for all components, which corresponds to the initial array displacements for the control input in Eq. (30), as explained in "Model setting". Therefore, the array displacements cannot be constrained using the observational data in this case. However, since the conventional array positioning method requires more than four responsive transponders to estimate the three components of the array

position and NTDs (orange crosses in Fig. 10), the EKF-based array positioning method can increase positioning opportunities when only three responsive transponders are available.

Improvements in the detection of vertical array displacements

As shown both in the synthetic tests (Figs. 4, 5) and in the actual observational data analysis (Fig. 8; Additional file 1: Figures S4–S8), the EKF-based array positioning method successfully improves the precision of the array displacements, especially for the vertical component when using multi-angled transponders. However, unlike the synthetic tests, the positioning results using the actual observational data showed temporal fluctuations in the vertical array displacements of up to a few tens of centimeters (Fig. 8c; Additional file 1: Figures S4c–S8c). The primary reasons for this temporal fluctuation are (1) GNSS positioning errors on the sea-surface platform, and (2) deviation from a laterally stratified SSS in the actual ocean. Note that Earth tide effects were eliminated in the shown vertical positioning results in advance although the Earth tide potentially produces long-term fluctuation in the vertical component.

The GNSS positioning errors directly propagate to the positions of the acoustic transducers on the sea-surface platform and then propagate to the array displacements. Although it is difficult to evaluate positioning errors for this moving body, we can consider that the vertical positions of the acoustic transducer on the sea-surface platform are inherently bounded to the sea surface. Therefore, eliminating oceanic tidal effects and geoid heights from the acoustic transducer positions, we can roughly evaluate the relative temporal fluctuation of the vertical GNSS positioning errors, although the absolute GNSS positioning errors cannot be evaluated (Fujita and Yabuki 2003). The vertical positions of the acoustic transducers are shown as bold gray curves in Fig. 8c and Additional file 1: Figures S4c–S8c, eliminating the oceanic tidal effects using the NAO.99Jb model (Matsumoto 2000) and the geoid heights calculated from Fukuda (1990). Note that the acoustic transducer positions are smoothed by a 5-min moving average filter because the positions are shaken by sea waves with short timescale. Since the long-term fluctuation in the vertical array positions is consistent with that of the acoustic transducer positions, the GNSS positioning errors are considered to be the major source of error in the vertical array displacements. Table 2 shows 1σ standard deviations of the vertical array positions for the actual observational data estimated by the conventional array positioning method (columns 3–5) and by the EKF-based array positioning method (columns 6–8). The average standard deviation of 11.14 cm (column 6: std.) is reduced to 9.18 cm (column 7: corrected std.) by subtracting the acoustic transducer positions in the case of the EKF-based array positioning method [the reduction can be up to ~5 cm in the observational data for G04 (March, 2015)]. Although one of the factors causing the long-term GNSS positioning errors is the very long baseline for kinematic differential GNSS positioning (e.g., Colombo et al. 2000), kinematic precise point positioning (PPP) (Zumberge et al. 1997) techniques, which do not require a terrestrial reference station, have improved and would be an alternative way of determining the position of the sea-surface platform. Watanabe et al. (2017) reported that kinematic PPP provided more stable solutions than long-baseline differential positioning. These developments in GNSS positioning would enable us to further improve the precision of the vertical array displacements using the EKF-based array positioning to less than ~10 cm. It should be noted that the precisions discussed here are relative precisions in the half-day observation data, and are not the absolute accuracy of the vertical positions. To discuss the absolute accuracy, much longer observational data are required.

In addition to long-term GNSS positioning errors, the vertical array displacements also have short-term variations with periods of ~tens of minutes (e.g., Figure 8c; Additional file 1: Figures S4c–S8c). These short-term variations may result from deviation from a laterally stratified SSS in the actual ocean. Although the horizontally graded SSS does not strongly affect positioning of the vertical array displacements as shown by the synthetic tests (Figs. 4, 5), more complicated spatial heterogeneity may affect the positioning of the vertical array displacements. In fact, the horizontal array displacements often fluctuate over similar time periods (Fig. 8; Additional file 1: Figures S4–S8). The GNSS positioning errors of the sea-surface platform possibly produced the short-term fluctuations in the vertical array displacements, but it is hard to evaluate their contributions. Since the positioning errors of the vertical array displacements appear to be systematic with time, detection of an abrupt step in the array position, such as a coseismic slip event, would be more precisely determined than a stable array displacement. To investigate the precision of the array displacements relative to the previous time step for detection of an abrupt step, we calculated differential sequences of the vertical array displacements and then calculated the standard deviation of the differential sequences (columns 5 and 8 in Table 2: difference std.). As a result, the standard deviation for the EKF-based array positioning method is on average 4.50 cm, while that of the conventional array positioning method is on average 9.13 cm. Since the EKF-based array positioning method constrains the temporal evolution of the NTDs, we can precisely

Table 2 1σ standard deviations (std.) of the vertical array displacements assuming a laterally stratified SSS

Site name	Date	Conventional array positioning			EKF-based array positioning		
		Std. (cm)	Corrected std. (cm)	Difference std. (cm)	Std. (cm)	Corrected std. (cm)	Difference std. (cm)
G04	September 22, 2012	10.23	7.32	4.41	10.05	7.02	3.15
G04	August 12, 2013	11.96	9.88	9.62	9.95	7.28	2.96
G04	November 4, 2013	12.50	10.72	4.17	12.10	10.24	2.44
G04	March 7, 2015	6.82	6.25	6.31	5.73	5.09	2.96
G04	November 3, 2015	7.13	7.98	5.34	6.48	7.48	3.85
G04	May 14, 2016	10.60	9.96	10.50	9.71	8.79	7.36
G10	September 13, 2012	17.83	14.30	12.81	14.18	8.29	3.93
G10	November 29, 2012	16.78	15.64	13.75	15.31	15.92	6.39
G10	July 29, 2013	14.95	12.13	8.27	13.54	10.87	3.94
G10	March 4, 2014	11.52	12.48	10.19	9.52	10.88	4.65
G10	September 20, 2014	8.43	7.08	5.40	8.09	6.45	3.14
G10	November 20, 2015	11.07	10.31	8.89	9.81	8.90	4.16
G10	May 20, 2016	13.65	12.35	9.98	12.50	11.25	5.73
G15	March 1, 2014	17.47	9.28	7.87	17.04	8.12	3.20
G15	November 9, 2015	10.99	11.70	11.02	8.12	8.97	3.97
G15	May 7, 2016	15.69	11.44	12.15	13.97	9.31	7.82
G19	September 6, 2012	13.47	12.40	10.58	14.59	16.00	5.85
G19	July 25, 2013	22.19	12.52	11.96	19.99	10.45	6.01
G19	February 26, 2014	11.23	8.46	5.87	10.83	7.94	3.59
G19	February 28, 2015	10.74	10.56	11.86	7.78	7.42	4.71
G19	November 15, 2015	9.22	8.07	8.27	7.97	6.50	4.24
G19	May 2, 2016	11.22	12.25	11.72	7.92	8.93	4.81
Average		12.53	10.59	9.13	11.14	9.18	4.50
Standard deviation		3.65	2.36	2.80	3.56	2.65	1.43

Columns 3 and 6 (std.) show simple standard deviations for solutions in the vertical component, while columns 4 and 7 (corrected std.) show standard deviations for solutions in the vertical component corrected by subtraction of the acoustic transducer positions. Columns 5 and 8 (difference std.) show standard deviations for differential sequences of the solutions in the vertical component

detect an abrupt step in the vertical component eliminating the potential trade-off relationship between the vertical array displacements and the NTDs.

Applicability to real-time GNSS-A positioning

Our main finding, accurate detection of vertical displacements, comes from appropriate estimation of NTDs constrained by the EKF. Although the constraint of temporal variations in NTDs can be achieved using conventional inversion techniques using a batch of acoustic ranging data (e.g., Honsho and Kido 2017), the EKF-based GNSS-A positioning method has an additional utility: instant processing suitable for real-time positioning.

The batch-type positioning requires high computational cost because a significant amount of data should be simultaneously processed; however, the EKF-based GNSS-A positioning method can determine a position using only acoustic ranging data for each ping, when the process noise values are fixed, as shown in "Results". In these circumstances, our method requires less computational cost, comparable to the simplest kinematic GNSS-A positioning methods which do not provide temporal constraints of NTDs (e.g., Spiess et al. 1998; Kido et al. 2006). Furthermore, the EKF-based positioning method can provide kinematic solutions instantly, just after collection of the acoustic ranging data for each ping, because this technique does not need "future" acoustic ranging data to constrain the temporal variation in NTDs. Recently, some trials of real-time and continuous GNSS-A observations have been conducted using a moored buoy (e.g., Imano et al. 2015; Kido et al. 2018; Kato et al. 2018; Tadokoro et al. 2018a). In this application, kinematic GNSS-A positions are estimated using a small computer attached to the buoy, which are then transmitted to an onshore station via satellite relay. Thus, the computational cost of GNSS-A positioning using a moored buoy is as low as possible. Our proposed method has a low computational cost and can provide a kinematic position with constraints on the temporal variation of NTDs, using real-time processing,

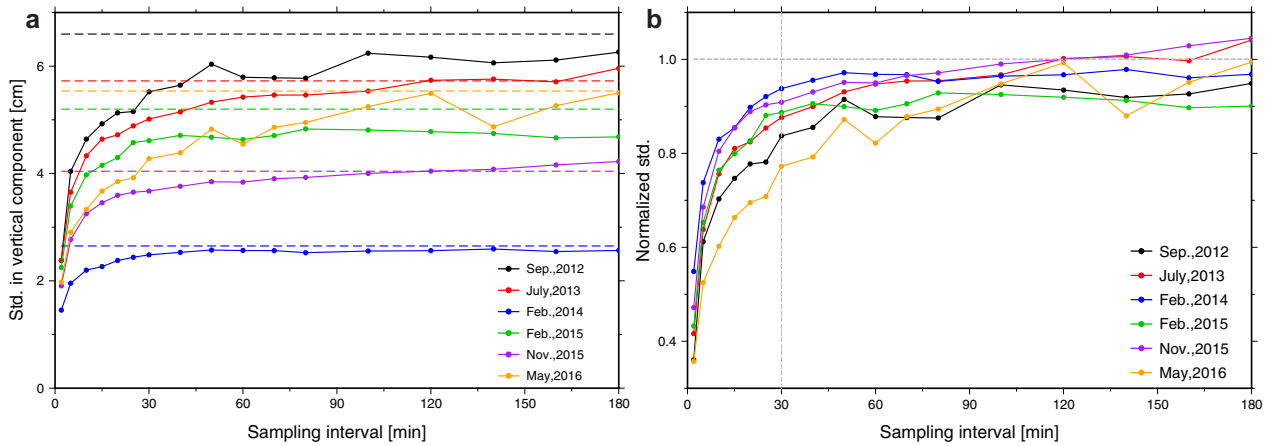

Fig. 11 Standard deviations in the vertical positions for various sampling intervals using actual observational data at G19. **a** Standard deviations in the vertical positions for various sampling intervals estimated using the EKF-based GNSS-A positioning method are shown by points and solid curves. Expected values for the standard deviations are the positions for the sampling interval of 60 s. Colors indicate the observation cruises. Dotted lines show RMSs of the vertical positions estimated using the classical GNSS-A positioning method. **b** The standard deviations shown in **a** are normalized by the positions estimated by the classical GNSS-A positioning method

making it suitable for real-time and continuous GNSS-A observations.

To estimate vertical positions using the EKF-based GNSS-A positioning method, frequency of acoustic ranging is an important factor to constrain the temporal variation NTDs. The recent yearly trials of GNSS-A observations using a moored buoy have performed acoustic ranging less frequency than campaigns using a research vessel, to conserve the battery life of the buoy and sensors. The interval of acoustic pings in the observations obtained using a research vessel are generally 30–60 s, whereas moored buoy systems provided a set of 11 acoustic pings with an interval of 65 s in a week (e.g., Imano et al. 2015; Kido et al. 2018), or acoustic ranging data with intervals of 180 s (e.g., Kato et al. 2018; Tadokoro et al. 2018a). In this study, we investigated the influence of sampling frequency on the vertical positioning using actual campaign observational data at site G19. We resampled the observational data for each campaign with various sampling intervals from 1 to 180 min, and then we estimated the kinematic positions using the EKF-based GNSS-A positioning using the optimal process noise for NTD (2.0×10^{-3} s/s$^{1/2}$). Figure 11a demonstrates standard deviations of the vertical positions for the different sampling intervals relative to those for the sampling interval of 60 s. Note that we consider that the most frequent sampling interval (here, 60 s) could provide the best solutions. Since the degree of improvement in the positioning is different from the cruise data, Fig. 11b shows the standard deviations normalized by those estimated using the classical GNSS-A positioning method without temporal smoothing for NTD. In most campaigns, the standard deviations for the sampling intervals longer than 30 min do not show clear difference, and they are close to those calculated using the classical kinematic positioning method (the normalized standard deviation is ~0.9). However, the standard deviations for the sampling intervals shorter than 30 min are significantly improved. Thus, a sampling interval shorter than 30 min should be used for continuous GNSS-A observations to obtain the most benefit from introduction of the EKF-based positioning method. Therefore, our method would provide usable constraints for acoustic ranging data with sampling intervals of a few minutes, such as those obtained using a moored buoy, while it would not be useful for the weekly interval of the acoustic ranging data (Imano et al. 2015; Kido et al. 2018). Since continuous GNSS-A observations using a moored buoy are still at the testing stage, specification of the system, such as sampling interval, can change. As long as the sampling interval is shorter than 30 min, it is worthwhile implementing our proposed method to continuous GNSS-A observation systems to obtain precise kinematic vertical positions.

Another issue that should be overcome for achieving the precise real-time GNSS-A positioning is how to keep the sea-surface platform position at the array center. Regardless of implementation of the EKF, the kinematic array positioning basically requires the point survey data because accuracy of the array displacements degrades away from the array center as explained in "Principles of the GNSS-A positioning method" (e.g., Kido 2007; Imano et al. 2015, 2019). In the past trials of the GNSS-A measurement using the moored buoy, the buoy

occasionally moved out of the transponder array, and the accuracy of the positioning was degraded (Imano et al. 2019). Thus, future technical improvement in operating the moored buoy is an important factor for the precise real-time GNSS-A positioning. This issue is beyond the scope of this study, but we emphasize that it is important to develop the both tangible (such as the moored buoy itself) and intangible (such as the EKF-based positioning method) factors.

Sound speed structure in actual ocean

Although the underwater delay gradients and the horizontal array displacements are well resolved in the synthetic test using the EKF-based array positioning method (Fig. 4), the horizontal array positions for the actual observational data fluctuate with time and deteriorate when compared to the solutions obtained assuming a laterally stratified SSS (Fig. 8). Although it is inherently difficult to resolve the underwater delay gradients and the horizontal array displacements due to their trade-off relationship, the numerical instability due to this trade-off should be random (as shown by the conventional array positioning method in the synthetic test: green diamonds in Fig. 5) rather than have a temporal fluctuation (as found from the actual observational data: purple circles in Fig. 8). Thus, we consider that the temporal fluctuations in the horizontal array displacements may be caused by systematic errors in modeling SSS not by numerical instability; SSS in the actual ocean might not be well expressed using horizontal grading. As Kido (2007) pointed out, spatial heterogeneity in SSS with long wavelengths can be expressed as a horizontally graded SSS even if multiple gradients exist across different water depths. Note that the long wavelength implies that the wavelength is longer than distance among acoustic path lines at the depth where the graded structure exists. However, spatial heterogeneity in SSS with short wavelengths cannot be expressed using a horizontally graded SSS. Thus, in our results, we think that the underwater delay gradients were overestimated for such temporally fluctuating short-wavelength spatial heterogeneities, and that the horizontal array displacements also fluctuated due to the overestimated underwater delay gradients.

We found that the SSS might have short-wavelength heterogeneities (shorter than the distance among acoustic path line), with short time periods (~ tens of minutes), whereas some previous studies have already successfully improved accuracy of the GNSS-A positioning assuming the long-lived horizontally graded SSS (e.g., Yasuda et al. 2017; Yokota et al. 2018). However, these previous studies performed static GNSS-A positioning using long-term (over hours) observational data collected from moving surveys. Therefore, we consider that the actual ocean has mixed spatio-temporal heterogeneities in SSS, comprising both short-term and short-wavelength heterogeneities, and long-term and long-wavelength heterogeneities. Accordingly, the static GNSS-A positioning has successfully modeled the long-term and long-wavelength heterogeneity of the SSS via moving surveys, while the kinematic GNSS-A positioning method has faced serious modeling errors due to the short-term and short-wavelength heterogeneities in the SSS, especially for the detection of precise horizontal array displacements. Since precise modeling of the short-term and short-wavelength heterogeneity of the SSS is important not only to improve accuracy of the kinematic GNSS-A positioning but also to further improve precision of the static GNSS-A positioning, further developments of SSS modeling techniques are required. The simplest way to model such short-wavelength heterogeneities in the SSS is to increase the number of seafloor transponders and the number of sea-surface platforms although the financial costs would be high. Otherwise, it would be helpful for precise GNSS-A positioning to understand the spatio-temporal behavior of the internal gravity wave. The internal wave has been considered to be a source of the short-term and short-wavelength heterogeneity in the SSS (e.g., Spiess et al. 1998). However, the detailed characteristics of the internal waves (such as spatial extents of the internal waves) have not been well investigated. Such oceanographic information would improve the design of the observation model and/or the system model for the EKF formulation, and would reduce the systematic modeling errors.

Conclusion

In this study, we developed the EKF-based kinematic GNSS-A array positioning method, and we investigated its performance using both the synthetic data and actual observational data. The synthetic tests demonstrated the superiority of the EKF-based array positioning methods when compared with the conventional array positioning methods, for both cases assuming a laterally stratified SSS and a horizontally graded SSS. Through analyses of the observational data, we found that using the EKF-based array positioning method and assuming a laterally stratified SSS significantly improved the precision of the array displacements, especially for the vertical component. The precision of the vertical array displacements is ~ 10 cm; the long-term GNSS positioning errors on a sea-surface platform and the short-term deviation of SSS from a laterally stratified SSS might reduce the precision of the vertical array displacements and contribute to temporal fluctuations. Thus, detection of an abrupt step, such as due to a coseismic slip event, would be carried out much

more precisely via the EKF-based array positioning, with precision of ~5 cm. Furthermore, the EKF-based array positioning method also demonstrated robust performance in the instance of unresponsive transponders. However, as for the actual observational data, the EKF-based array positioning method, assuming a horizontally graded SSS, produced apparent fluctuations in the horizontal array displacements that made the precision worse than the results obtained assuming a laterally stratified SSS. These apparent fluctuations may be caused by short-wavelength spatial heterogeneities in the SSS; therefore, modeling such heterogeneities would be important to enable precise kinematic GNSS-A array positioning.

Supplementary information

Supplementary information accompanies this paper at https://doi.org/10.1186/s40623-019-1082-y.

Additional file 1: Figure S1. Schematic image of GNSS-A positioning bias caused by a horizontally graded sound speed structure. **Figure S2.** Schematic image of GNSS-A positioning through moving and point surveys. **Figure S3.** 2-D schematic image of seafloor transponder arrangements. **Figure S4.** Positioning results for the actual observation data at G19 on September 6, 2012. **Figure S5.** Positioning results for the actual observation data at G19 on July 25, 2013. **Figure S6.** Positioning results for the actual observation data at G19 on February 26, 2014. **Figure S7.** Positioning results for the actual observation data at G19 on November 15, 2015. **Figure S8.** Positioning results for the actual observation data at G19 on May 2, 2016.

Abbreviations

EKF: extended Kalman filter; GNSS: Global Navigation Satellite System; GNSS-A: combination of Global Navigation Satellite System and Acoustic ranging; KF: Kalman filter; NTD: Nadir total delay; PPP: precise point positioning; SSS: sound speed structure; WOA13: World Ocean Atlas 2013; ZTD: zenith total delay.

Acknowledgements

We acknowledge Dr. Y. Ohta for his helpful comment on designing the study. We thank two anonymous reviewers and the editor Takuya Nishimura for providing us valuable comments to improve the manuscript. The figures were generated using Generic Mapping Tools software (Wessel and Smith 1998). We thank Editage (www.editage.jp) for English language editing.

Authors' contributions

FT analyzed all the calculations shown in this study and drafted the manuscript including figure. MK, CH, and RM contributed to discussion and interpretation, and they improved the developed technique and the manuscript. All authors read and approved the final manuscript.

Funding

This research was supported by Ministry of Education, Culture, Sports, Science and Technology (MEXT; Grant Number: 1222), Japan in the Project for "Development of GPS/Acoustic Technique" and by Japan Science and Technology Agency (JST) with Council for Science, Technology and Innovation (CSTI), Cross-ministerial Strategic Innovation Promotion Program (SIP) "Enhancement of societal resiliency against natural disasters", and by Japan Society for the Promotion of Science (JSPS) KAKENHI (Grant Number: 17J026523).

Availability of data and materials

The original data and findings of this study are available from the corresponding author upon a reasonable request.

Ethics approval and consent to participate

Not applicable.

Consent for publication

Not applicable.

Competing interests

The author declares that they have no competing interests.

Author details

[1] Graduate School of Science, Hokkaido University, Sapporo, Japan. [2] Present Address: Japan Agency for Marine-Earth Science and Technology, Yokohama, Japan. [3] International Research Institute of Disaster Science, Tohoku University, Sendai, Japan. [4] Graduate School of Science, Tohoku University, Sendai, Japan.

Received: 20 April 2019 Accepted: 14 September 2019
Published online: 23 September 2019

References

Bar-Server YE, Kroger PM, Borjesson JA (1998) Estimating horizontal gradients of tropospheric path delay with a single GPS receiver. J Geophys Res Solid Earth 103(B3):5019–5035. https://doi.org/10.1029/97JB03534

Chadwell CD, Spiess FN (2008) Plate motion at the ridge-transform boundary of the south Cleft segment of the Juan de Fuca Ridge from GPS-Acoustic data. J Geophys Res Solid Earth 113:B04415. https://doi.org/10.1029/2007JB004936

Chen CT, Millero FJ (1977) Speed of sound in seawater at high pressures. J Acoust Soc Am 62:1129–1135

Chen H-Y, Ikuta R, Lin C-H, Hsu Y-J, Kohmi T, Wang C-C, Yu S-B, Tu Y, Tsujii T, Ando M (2018) Back-Arc opening in the western end of the Okinawa trough revealed from GNSS/Acoustic measurements. Geophys Res Lett 45:137–145. https://doi.org/10.1002/2017GL075724

Colombo OL, Evans AG, Vigo-Aguiar MI, Ferrandiz JM, Benjamin JJ (2000) Long-baseline (> 1000 km), sub-decimeter kinematic positioning of Buoys at sea, with potential application to deep-sea studies. In: the ION GPS 2000 meeting (September), pp 1476–1484

Fujimoto H (2014) Seafloor geodetic approaches to subduction thrust earthquakes. Monogr Environ Earth Planets 2(2):23–63. https://doi.org/10.5047/meep.2014.00202.0023

Fujita M, Yabuki T (2003) A way of accuracy estimation of K-GPS results in the seafloor geodetic measurement. Tech Bull Hydrogr Oceanogr 21:62–66 **(in Japanese)**

Fujita M, Ishikawa T, Mochizuki M, Sato M, Toyama S, Katayama M (2006) GPS/Acoustic seafloor geodetic observation: method of data analysis and its application. Earth Planets Space 58(3):265–275. https://doi.org/10.1186/BF03351923

Fukuda Y (1990) Precise determination of local gravity field both the satellite altimeter data and the surface gravity data. Bull Ocean Res Inst Univ Tokyo 133:1–33

Gagnon K, Chadwell CD, Norabuena E (2005) Measuring the onset of locking in the Peru-Chile trench with GPS and acoustic measurements. Nature 434(7030):205–208. https://doi.org/10.1038/nature03412

Herring TA, Davis JL, Shapiro II (1990) Geodesy by radio interferometry: the application of Kalman filtering to the analysis of very long baseline interferometry data. J Geophys Res Solid Earth 95(B8):12561–12581. https://doi.org/10.1029/JB095iB08p12561

Hirata N, Matsu'ura M (1987) Maximum-likelihood-estimation of hypocenter with origin time eliminated using nonlinear inversion technique. Phys Earth Planet Inter 47:50–61. https://doi.org/10.1016/0031-9201(87)90066-5

Hirata Y, Ohta Y (2016) Spatial and temporal characteristics of optimum process noise values of tropospheric parameters for kinematic analysis of global navigation satellite system (GNSS) sites in Japan. Earth Planets Space 68(1):203. https://doi.org/10.1186/s40623-016-0578-y

Honsho C, Kido M (2017) Comprehensive analysis of traveltime data collected through GPS-acoustic observation of seafloor crustal movements. J Geophys Res. https://doi.org/10.1002/2017JB014733

Honsho C, Kido M, Tomita F, Uchida N (2019) Offshore postseismic deformation of the 2011 Tohoku earthquake revisited: application of an improved GPS-acoustic positioning method considering horizontal gradient of sound speed structure. J Geophys Res Solid Earth. https://doi.org/10.1029/2018JB017135

Ikuta R, Tadokoro K, Ando M, Okuda T, Sugimoto S, Takatami K, Yada K, Besana GM (2008) A new GPS-acoustic method for measuring ocean floor crustal deformation: application to the Nankai Trough. J Geophys Res Solid Earth 113:B02401. https://doi.org/10.1029/2006JB004875

Imano M, Kido M, Ohta Y, Fukuda T, Ochi H, Takahashi N, Hino R (2015) Improvement in the accuracy of real-time GPS/acoustic measurements using a multi-purpose moored buoy system by removal of acoustic multipath. In: Hashimoto M (ed) International association of geodesy symposia (GENAH), International Association of Geodetic Symposia, vol 145. Springer, Cham. https://doi.org/10.1007/1345_2015_192

Imano M, Kido M, Honsho C, Ohta Y, Takahashi N, Fukuda T, Ochi H, Hino R (2019) Assessment of directional accuracy of GNSS-Acoustic measurement using a slackly moored buoy. Prog Earth Planet Sci. https://doi.org/10.1186/s40645-019-0302-1

Kalman RE (1960) A new approach to linear filtering and prediction problems. J Basic Eng 81(1):35–45

Kato T, Terada Y, Tadokoro K, Kinugasa N, Futamura A, Toyoshima M, Yamamoto S, Ishii M, Tsugawa T, Nishioka M, Takizawa K, Shoji Y, Seko H (2018) Development of GNSS buoy for a synthetic geohazard monitoring system. J Disaster Res 13(3):460–471. https://doi.org/10.20965/jdr.2018.p0460

Kido M (2007) Detecting horizontal gradient of sound speed in ocean. Earth Planets Space 59(12):33–36

Kido M, Fujimoto H, Miura S, Osada Y, Tsuka K, Tabei T (2006) Seafloor displacement at Kumano-nada caused by the 2004 off Kii Peninsula earthquakes, detected through repeated GPS/acoustic surveys. Earth Planets Space 58(7):911–915. https://doi.org/10.1186/BF03351996

Kido M, Osada Y, Fujimoto H (2008) Temporal variation of sound speed in ocean: a comparison between GPS/acoustic and in situ measurements. Earth Planets Space 60:229–234. https://doi.org/10.1186/BF03352785

Kido M, Osada Y, Fujimoto H, Hino R, Ito Y (2011) Trench-normal variation in observed seafloor displacements associated with the 2011 Tohoku-Oki earthquake. Geophys Res Lett 38:L24303. https://doi.org/10.1029/2011GL050057

Kido M, Fujimoto H, Hino R, Ohta Y, Osada Y, Iinuma T, Azuma R, Wada I, Miura S, Suzuki S, Tomita F, Imano M (2015) Progress in the project for development of GPS/acoustic technique over the last 4 years. In: Hashimoto M (ed) International association of geodesy symposia (GENAH), International Association of Geodetic Symposia, vol 145. Springer, Cham. https://doi.org/10.1007/1345_2015_127

Kido M, Imano M, Ohta Y, Fukuda T, Takahashi N, Tsubone S, Ishihara Y, Ochi H, Imai K, Honsho C, Hino R (2018) Onboard realtime processing of GPS-Acoustic data for moored buoy-based observation. J Disaster Res. https://doi.org/10.20965/jdr.2018.p0472

Kitagawa G (2005) Introduction to time series analysis. Iwakuni Shoten, Japan **(in Japanese)**

Lichten SM, Border JS (1987) Strategies for high-precision global positioning system orbit determination. J Geophys Res 92(B12):12751–12762. https://doi.org/10.1029/JB092iB12p12751

Locarnini RA, Mishonov AV, Antonov JI, Boyer TP, Garcia HE, Baranova OK, Zweng MM, Paver CR, Reagan JR, Johnson DR, Hamilton M, Seidov D (2013) World ocean atlas 2013, Volume 1: temperature. Levitus S, Mishonov Technical A (eds), NOAA Atlas NESDIS, 73, p 40

MacMillan DS (1995) Atmospheric gradients from very long baseline interferometry observations. Geophys Res Lett 22(9):1041–1044. https://doi.org/10.1029/95GL00887

Marini JW (1972) Correction of satellite tracking data for an arbitrary tropospheric profile. Radio Sci 7(2):223–231

Matsumoto K (2000) Ocean tide models developed by assimilating TOPEX/POSEIDON altimeter data into hydrodynamical model: a global model and a regional model around Japan. J Oceanogr 56:567–581

Matsumoto Y, Fujita M, Ishikawa T (2008) Development of multi-epoch method for determining seafloor station position. Tech Bull Hydrogr Oceanogr 26:16–22 **(in Japanese)**

Sato M, Ishikawa T, Ujihara N, Yoshida S, Fujita M, Mochizuki M, Asada A (2011) Displacement above the hypocenter of the 2011 Tohoku-Oki earthquake. Science 332(6036):1395. https://doi.org/10.1126/science.1207401

Sato M, Fujita M, Matsumoto Y, Saito H, Ishikawa T, Asakura T (2013) Improvement of GPS/acoustic seafloor positioning precision through controlling the ship's track line. J Geodesy 87(9):825–842. https://doi.org/10.1007/s00190-013-0649-9

Segall P, Matthews M (1997) Time dependent inversion of geodetic data. J Geophys Res 102(B10):22391. https://doi.org/10.1029/97JB01795

Spiess FN (1985) Suboceanic geodetic measurements. IEEE Trans Geosci Remote Sens 23(4):502–510

Spiess FN, Chadwell CD, Hildebrand JA, Young LE, Purcell GH, Dragert H (1998) Precise GPS/acoustic positioning of seafloor reference points for tectonic studies. Phys Earth Planet Inter 108(2):101–112. https://doi.org/10.1016/S0031-9201(98)00089-2

Sugimoto S, Osada Y, Ishikawa T, Asakura T, Tadokoro K, Watanabe T, Okuda T, Takatani K, Ikuta R, Ando M (2009) Evaluation of kinematic GPS software based on experiment of positioning for moving object with various baseline length. J Geodetic Soc Jpn 55(1):65–85 **(in Japanese)**

Tadokoro K, Ando M, Ikruta R, Okuda T, Besana GM, Sugimoto S, Kuno M (2006) Observation of coseismic seafloor crustal deformation due to M7 class offshore earthquakes. Geophys Res Lett 33:L23306. https://doi.org/10.1029/2006GL026742

Tadokoro K, Ikuta R, Watanabe T, Ando M, Okuda T, Nagai S, Yasuda K, Sakata T (2012) Interseismic seafloor crustal deformation immediately above the source region of anticipated megathrust earthquake along the Nankai Trough, Japan. Geophys Res Lett 39:L10306. https://doi.org/10.1029/2012GL051696

Tadokoro K, Kinugasa N, Kato T, Terada Y (2018a) Experiment of acoustic ranging from GNSS buoy for continuous seafloor crustal deformation measurement. AGU Fall Meeting 2018, T41F-0361, Washington D.C., Dec. 2018

Tadokoro K, Nakamura M, Ando M, Kimura H, Watanabe T, Matsuhiro K (2018b) Interplate coupling state at the Nansei-Shoto (Ryukyu) Trench, Japan, deduced from seafloor crustal deformation measurements. Geophys Res Lett. https://doi.org/10.1029/2018GL078655

Tomita F, Kido M, Osada Y, Hino R, Ohta Y, Iinuma T (2015) First measurement of the displacement rate of the Pacific Plate near the Japan Trench after the 2011 Tohoku-Oki earthquake using GPS/acoustic technique. Geophys Res Lett 42(20):8391–8397. https://doi.org/10.1002/2015GL065746

Tomita F, Kido M, Ohta Y, Iinuma T, Hino R (2017) Along-trench variation in seafloor displacements after the 2011 Tohoku earthquake. Sci Adv 3:e1700113. https://doi.org/10.1126/sciadv.1700113

Watanabe S, Sato M, Fujita M, Ishikawa T, Yokota Y, Ujihara N, Asada A (2014) Evidence of viscoelastic deformation following the 2011 Tohoku-Oki earthquake revealed from seafloor geodetic observation. Geophys Res Lett 41:5789–5796

Watanabe S, Bock Y, Chadwell CD, Fang P, Geng J (2017) Long-term stability of the kinematic precise point positioning for the sea surface observation unit compared with the baseline analysis. Tech Bull Hydrogr Oceanogr 54:38–73

Wessel P, Smith WHF (1998) New, improved version of the generic mapping tools released. Eos Trans AGU 79:579

Yasuda K, Tadokoro K, Taniguchi S, Kimura H, Matsuhiro K (2017) Interplate locking condition derived from seafloor geodetic observation in the shallowest subduction segment at the Central Nankai Trough, Japan. Geophys Res Lett 44:3572–3579. https://doi.org/10.1002/2017GL072918

Yokota Y, Ishikawa T, Watanabe S, Tashiro T, Asada A (2016) Seafloor geodetic constraints on interplate coupling of the Nankai Trough megathrust zone. Nature 534(7607):374–377. https://doi.org/10.1038/nature17632

Yokota Y, Ishikawa T, Watanabe S (2018) Gradient field of undersea sound speed structure extracted from the GNSS-A oceanography. Mar Geophys Res. https://doi.org/10.1007/s11001-018-9362-7

Zumberge JF, Heflin MB, Jefferson DC, Watkins MM, Webb FH (1997) Precise point positioning for the efficient and robust analysis of GPS data from large networks. J Geophys Res Solid Earth 102(B3):5005–5017. https://doi.org/10.1029/96JB03860

Zweng MM, Reagan JR, Antonov JI, Locarnini RA, Mishonov AV, Boyer TP, Garcia HE, Baranova OK, Johnson DR, Seidov D, Biddle MM (2013) World ocean atlas 2013, volume 2: salinity. Levitus S, Mishonov Technical A (eds). NOAA Atlas NESDIS, vol 74, p 39

Publisher's Note